Histone variant H2BE enhances chromatin accessibility in neurons to promote synaptic gene expression and long-term memory

Emily R. Feierman[1,3,4], Sean Louzon[2,3,4], Nicholas A. Prescott[6,7], Tracy Biaco[6,7], Qingzeng Gao[6], Qi Qiu[3], Kyuhyun Choi[5], Katherine C. Palozola[3,4], Anna J. Voss[1,3,4], Shreya Mehta[3,4], Camille Quaye[3,4], Katherine Lynch[3,4], Marc Fuccillo[5], Hao Wu[3,4], Yael David[6,7], Erica Korb[3,4]*

[1]Neuroscience Graduate Group, [2]Cell and Molecular Biology Graduate Group, [3]Department of Genetics, [4]Epigenetics Institute, [5]Department of Neuroscience, University of Pennsylvania Perelman School of Medicine, Philadelphia, PA, [6]Chemical Biology Program, Memorial Sloan Kettering Cancer Center, [7]Tri-institutional PhD Program in Chemical Biology, New York, NY, *corresponding author ekorb@pennmedicine.upenn.edu

ABSTRACT

Regulation of histones occurs through multiple mechanisms including exchange with histone variants. Unlike canonical histones, variants are replication-independent and therefore accumulate in post-mitotic cells such as neurons. While recent findings link variants to neurological and neuropsychiatric disorders, few are well studied in the context of the brain. H2BE is the single H2B variant found outside germline tissues, yet its expression and effects on chromatin remained unclear. We applied new tools including novel antibodies, biochemical assays, and sequencing approaches to reveal broad H2BE expression in the brain and its role in regulating chromatin structure, neuronal transcription, and mouse behavior. H2BE is enriched at promoters and enhances chromatin accessibility. We further identify a single amino acid driving these accessibility changes. Lastly, we show that H2BE is critical for synaptic gene expression and long-term memory. Together, these data reveal a novel mechanism linking histone variants to chromatin regulation and neuronal function underlying memory.

INTRODUCTION

Dynamic regulation of transcription is an integral part of a neuron's ability to form functional synapses and store information. Chromatin, the structure of DNA wrapped around histone proteins, allows cells in the brain to translate diverse environmental signals into a transcriptional profile that supports long-lasting memories and adaptive behavioral responses[1–3]. As a result, disruption of mechanisms that regulate chromatin and transcription has widespread effects and can lead to the onset of several neurological disorders, including autism spectrum disorder and related neurodevelopmental disorders[4–9] and neurodegeneration[10–13]. However, the molecular mechanisms through which histone proteins mediate complex neuronal functions such as memory formation are not fully understood.

Histone proteins are the central components of chromatin, affecting DNA compaction and thus, transcription. Two copies of each of the canonical histone proteins—H2A, H2B, H3, and H4—form an octamer around which

40 ~146 base pairs of DNA are wound[14]. Chromatin is regulated by the addition of post-translational modifications
41 onto histones and by expression of histone variants. Histone variants, which are encoded by separate genes,
42 can substitute for the canonical forms, and are involved in regulation of many cellular processes and gene
43 expression[15]. While canonical histone proteins are transcribed and translated during S phase of the cell cycle
44 and deposited concurrently with DNA replication[16], histone variants are unique in that they can be synthesized
45 throughout the cell cycle and continue to be generated and deposited into chromatin throughout the lifespan
46 of terminally-differentiated cells[17,18]. This feature makes histone variants particularly critical to post-mitotic cells
47 such as neurons. To date, several histone variants have been implicated in neuronal function and regulation of
48 neuronal transcription[10,19–26]. Changes in the expression of histone variants have been observed in animals
49 following exposure to diverse environmental factors including drugs of abuse[27] and social stress[23].

50 While variants of H2A and H3 are well characterized, few studies have investigated variants of histone H2B in
51 animals. A recent study identified seven mammalian H2B variants[28]. Of those, only one known variant, H2BE, is
52 expressed outside of germline tissues. The histone variant H2BE was discovered in the mouse main olfactory
53 epithelium, where it affects neuronal longevity and olfactory neuron function[29]. This study concluded that H2BE
54 was only expressed in olfactory epithelial neurons based on transcript expression data and that this remarkable
55 mechanism was a unique feature of the atypical cell turnover that occurs within this sensory system. However,
56 due to a lack of a specific antibody, analysis of H2BE protein expression could not be performed and limited
57 sequencing approaches available at the time precluded analysis of the mechanisms through which H2BE
58 regulates chromatin. While emerging evidence demonstrates the importance of histone variants in the brain
59 and in neurological disorders[10,19–26], to the best of our knowledge no subsequent studies have been published
60 in the intervening decade. Thus, whether H2BE is expressed outside of the olfactory system and how this
61 unusual protein affects chromatin and cellular functions beyond olfaction has remained a mystery.

62 Here, we sought to define the function of H2BE in regulating chromatin and examine whether it functions
63 beyond the olfactory epithelium. We generated a highly specific antibody for H2BE, allowing for comprehensive

64 analysis of H2BE throughout the brain. In addition, we combine biochemistry, mouse models, and animal
65 behavior with combinatorial analysis of various next-generation sequencing datasets to characterize genomic
66 localization of H2BE as well as its effects on chromatin structure, neuronal transcription, and cognition. We show
67 that H2BE is expressed throughout the brain. In neurons, H2BE is expressed at gene promoters, conferring an
68 open chromatin conformation. Further, we localize the major effects of H2BE on chromatin to a single amino
69 acid. Loss of H2BE results in widespread compaction of chromatin and transcriptional disruption leading to
70 synaptic dysfunction and impaired long-term memory. In summary, this work reveals a novel mechanism by
71 which a histone variant contributes to the complex chromatin environment in the brain, and links single amino
72 acid changes in histone proteins to regulation of neuronal transcription and cognition.

73 **RESULTS**

74 **H2BE is expressed at promoters in cortical neurons**

75 The histone variant H2BE differs from its canonical counterpart, H2B, by only five amino acids. The five amino
76 acid changes in H2BE are distributed throughout the length of the protein, with one in each tail and three that
77 lie within the globular domain (Fig 1a). A major challenge to studying this variant has been the lack of tools to
78 directly and specifically detect endogenous H2BE protein. To overcome this, through a partnership with
79 MilliporeSigma, we developed and tested a highly specific antibody against the first ten amino acids at the N-
80 terminal of H2BE. This antibody has no cross-reactivity to canonical H2B or H3 tail peptides (Supp Fig 1a). To
81 further confirm the specificity of the antibody, we obtained the previously reported H2BE knockout (KO)
82 mouse[29], in which the coding sequence of *H2bc21* was replaced with a membrane-targeted mCherry reporter
83 sequence (Supp Fig 1b). We confirmed the loss of H2BE transcript using RNA-sequencing of WT and KO primary
84 cortical neurons (Supp Fig 1c). As previously reported[29], KO mice are viable and heterozygous crosses generate
85 expected Mendelian ratios (Supp Fig 1d).

86 We extracted histones from adult mouse brain tissue and detected H2BE in the cortex, hippocampus, and
87 cerebellum of WT mice (Fig 1b) indicating much more widespread expression than previously reported.
88 Importantly, we observed no signal in any KO tissue demonstrating antibody specificity in tissue. We also
89 measured H2BE in whole protein lysates from WT and KO cortical tissue and primary cultured neurons derived
90 from E16.5 embryonic cortices and similarly observed H2BE expression in WT tissue and cultured neurons with
91 no detectable signal in KOs (Supp Fig 1e-f). We further confirmed specificity using immunohistochemistry of WT
92 and KO sections of adult mice (Supp Fig 1g) and found that H2BE co-localizes with the neuronal marker NeuN
93 (Fig 1c), confirming the expression of H2BE in neurons *in vivo*. H2BE is also present in several tissues throughout
94 the body but enriched in the brain relative to other tissues (Supp Fig 1h). We also found high levels of H2BE
95 expression in the main olfactory epithelium consistent with previous findings originally identifying H2BE
96 transcript as highly enriched in this tissue[29]. These data provide the first characterization of H2BE protein
97 expression, and importantly, demonstrate that it is expressed outside the olfactory system with detectable
98 levels throughout the mouse brain. This expands the relevance of H2BE beyond what was previously believed
99 to be a variant exclusively expressed in sensory neurons of the olfactory epithelium. Further, while H2A and H3
100 variants are now well characterized in multiple cell types, this analysis of H2BE expression provides the first
101 evidence of an H2B variant that is widely expressed in multiple tissues.

102 We next assessed the abundance of H2BE relative to the total pool of H2B in mouse cortex. H2BE was nearly
103 absent in the cortex at birth, while its abundance increased over time and reached 0.24% of all H2B species by
104 adulthood (Fig 1d; Supp Fig 1i). This low percentage is notable given that other histone proteins such as H3.3
105 and H2A.Z accumulate in post-mitotic cells such as neurons and become the dominant species[19,22]. However,
106 histone variants can also have specific genomic enrichment patterns[9,19,22,30–33]. We therefore speculated that if
107 H2BE is concentrated in specific genomic locations, this would allow it to exert significant effects on chromatin
108 while only accounting for a small percentage of the total H2B protein pool. To test this, we performed CUT&Tag
109 with sequencing[34] on primary cortical neurons from WT and KO E16.5 embryos following 12 days in culture. We

110 first validated our antibody for CUT&Tag by comparing enrichment of H2BE signal over background signal in KO
111 cells (Supp Fig 1j) and by confirming a high concordance of peak sites between replicates (Supp Fig 1k). We
112 found that H2BE expression is highly enriched in core promoter regions throughout the genome (Fig 1e-f; Supp
113 Fig 1l) with most identified peaks near a transcription start site (TSS) (Fig 1g). Gene ontology analysis shows that
114 H2BE is enriched specifically at genes related to important neuronal functions, including dendrite
115 morphogenesis, synaptic vesicle endocytosis, and others (Supp Fig 1m). Further, H2BE enrichment is positively
116 correlated with gene expression in WT neurons (Fig 1h-k), suggesting a relationship between H2BE enrichment
117 and expression of neighboring genes. Together, these data indicate that H2BE is expressed at low levels relative
118 to other H2B proteins in the mouse cortex but is highly enriched at core promoters, a regulatory region critical
119 for the control of gene transcription.

120 **H2BE promotes open chromatin via interactions at the histone-DNA interface**

121 H2BE has 3 unique amino acids that lie within the globular domain. Of these, asparagine at position 75 (N75)
122 and serine at position 97 (S97) are embedded within the nucleosome core, while the isoleucine at site 39 (I39)
123 lies within the histone-DNA interface[14] (Fig 1a). Due to the location of these amino acids within the nucleosome
124 core (N75 and S97), we tested whether H2BE affects nucleosome stability. We generated nucleosomes
125 containing either two copies of canonical H2B or variant H2BE with canonical H2A, H3, and H4. Importantly,
126 there were no changes in thermal stability between H2B- and H2BE-containing nucleosomes. Both species
127 yielded two melting peaks at ~72 °C (Tm1) and ~85 °C (Tm2) corresponding to H2A/H2B dimer and H3/H4
128 tetramer dissociation, respectively (Fig 2a). This indicates that H2BE-specific amino acids do not affect
129 nucleosome stability.

130 We next tested the ability of H2BE to compact DNA due to the H2BE-specific amino acid located at the DNA
131 interface (I39). Nucleosome arrays were generated by combining H2B- or H2BE-containing octamers with
132 12x601 DNA and compaction was measured using atomic force microscopy[35]. We found that canonical H2B-
133 containing arrays occupy a smaller surface area compared to H2BE-containing arrays (Fig 2b-c), without a

134 change in volume of the nucleosomes (Supp Fig 2a), demonstrating that the incorporation of H2BE confers a
135 more open chromatin conformation relative to canonical H2B. To confirm these findings, we used Mg^{2+}
136 precipitation assays[36] and found that H2BE arrays display a lower propensity to oligomerize in the presence of
137 increasing concentrations of Mg^{2+} (Supp Fig 2b). Together, these assays revealed that H2BE nucleosome arrays
138 are qualitatively more open compared to H2B arrays without affecting nucleosome stability. Further, these data
139 indicate that the effect of H2BE on chromatin compaction is intrinsic to the amino acid sequence of the protein
140 as the only components present in these *in vitro* assays include unmodified histones and DNA without other
141 protein complexes or the addition of histone post translational modifications. Thus, the effect of H2BE in
142 decreasing chromatin compaction occurs irrespective of posttranslational modifications and cellular signaling
143 mechanisms and is an innate property of H2BE.

144 These biochemical assays were performed using synthetic nucleosomes containing 2 copies of either canonical
145 H2B or H2BE. However, in a cellular context, it is possible that H2BE coexists with H2B in a nucleosome. We
146 therefore assessed the effect of H2BE on chromatin accessibility in a physiological context using WT and KO
147 primary cortical neurons paired with the assay for transposase-accessible chromatin with sequencing (ATAC-
148 seq)[37]. We first performed an analysis of chromatin accessibility at accessible genomic regions including
149 transcription start sites (TSSs) and enhancers in an unbiased fashion regardless of whether a peak was detected
150 in WT neurons. We found a decrease in accessibility in KO neurons at TSSs (Supp Fig 2c-e). Of all TSSs with
151 differential accessibility in KO, 99.98% (8,559 sites) were downregulated, while only 0.02% (2 sites) were
152 upregulated. We observed a similar decrease in accessibility at enhancer regions (Supp Fig 2f-h), with no sites
153 showing significantly increased accessibility. We also examined accessibility genome-wide, focusing on peaks
154 detected in WT neurons regardless of genomic region, and again found that loss of H2BE results in marked
155 decreased chromatin accessibility (Fig 2d-g; Supp Fig 2i-j).

156 To determine the relationship between H2BE enrichment and chromatin accessibility, we measured ATAC-seq
157 signal at all H2BE peaks identified by CUT&Tag. H2BE peaks showed decreased accessibility in KO neurons (Fig

158 2h-k). Of all H2BE peaks, 53.2% had decreased accessibility in KO, and zero had increased accessibility (Fig 2k).
159 Further, we found that sites with the greatest enrichment of H2BE in WT neurons also showed the greatest
160 magnitude change in ATAC signal between WT and KO, suggesting a direct correlation between H2BE occupancy
161 and chromatin compaction upon H2BE loss (Fig 2l-n). We then subset H2BE peaks by genomic region and
162 quantified the number of peaks with decreased accessibility in KO. We found that 77.5% H2BE-bound
163 transcription start sites had decreased accessibility, while more modest changes were observed at H2BE peaks
164 in the gene body (40.3%) and in intergenic H2BE peak regions (28.0%) (Supp Fig 2k-l). These data demonstrate
165 a direct role of H2BE in modulating chromatin accessibility in neurons, particularly at transcription start sites.

166 We speculated that the amino acid difference found at I39 drives the effects on chromatin accessibility based
167 on its location at the nucleosome-DNA interface (Fig 3a). To test the necessity and sufficiency of this single
168 amino acid for the effect of H2BE on accessibility, we generated mutant nucleosomes in which the H2BE-specific
169 isoleucine at site 39 is mutated to valine (H2BE-I39V), the amino acid found at that site on canonical H2B, and
170 the converse where the valine at site 39 on canonical H2B was converted to isoleucine (H2B-V39I) (Fig 3b, Supp
171 Fig 3a). We then measured thermal stability of the mutant nucleosomes and detected no differences between
172 H2B, H2BE, H2BE-I39V, and H2B-V39I nucleosomes (Fig 3c). We then constructed chromatin arrays from these
173 nucleosomes (Supp Fig 3b) and measured compaction with a Mg^{2+} precipitation assay. We found that arrays
174 containing H2BE-I39V are less soluble than WT H2BE arrays in the presence of Mg^{2+}, indicating that H2BE-I39V
175 are more compact than H2BE arrays (Fig 3d). Further, the V39I mutation on canonical H2B was sufficient to
176 make H2B-V39I nucleosome arrays more soluble than arrays containing WT H2B (Fig 3e). Together, these data
177 demonstrate that the I39 on H2BE is both necessary and sufficient for H2BE to promote open chromatin. Finally,
178 we generated viral vectors containing WT H2BE or mutant H2BE-I39V and used these viruses to re-express H2BE
179 in KO neurons (Supp Fig 3c). We then performed ATAC-seq to measure global changes in accessibility. As we
180 previously showed, WT neurons have more open chromatin than KO neurons. We confirmed that these results
181 were not simply due to viral infection or overexpression of a histone using a virus expressing a GFP reporter only

182 or canonical H2B, respectively. We also found that re-expressing WT H2BE was sufficient to open chromatin
183 around the TSS. In contrast, neurons expressing I39V mutants were indistinguishable from KO neurons (Fig 3f-
184 g). Taken together, these data illustrate that this amino acid is necessary for the effect of H2BE on chromatin
185 compaction.

186 **H2BE promotes synaptic gene expression**

187 Given the profound changes detected in chromatin accessibility in KO neurons, we next performed RNA-
188 sequencing (RNA-seq) on WT and KO primary cortical neurons to determine how loss of H2BE affects gene
189 expression. We saw broad changes in gene expression in KO neurons, with 1,790 downregulated genes and
190 1,764 upregulated genes (Fig 4a). We note that *H2bc21* is called as upregulated in KO in our differential
191 expression analysis because of signal mapping to the 3'UTR located downstream of the H2BE coding sequence
192 (Supp Fig 1d). In the KO, the H2BE coding sequence is replaced by mCherry[29] allowing for continued expression
193 of the UTR and has therefore been removed from further analysis. Downregulated genes are enriched for
194 functions related to neuronal morphology and axon growth while upregulated genes are enriched for functions
195 related to cellular metabolism and mitochondrial function (Fig 4b). Because many of the downregulated genes
196 were related to synapse function, we also analyzed differentially expressed genes with SynGO[39] which
197 confirmed disruption of critical synaptic functions particularly those related to regulation of synaptic
198 transmission and signaling (Supp Fig 4a).

199 To better understand the properties of differentially expressed genes, we looked at basal expression levels in
200 WT of genes that were downregulated, upregulated, or unaffected in KO. We found that genes that were
201 downregulated in KO had higher expression in WT cells compared to both upregulated genes and non-
202 differentially expressed genes (Fig 4c). These data suggest that highly expressed genes are more susceptible to
203 downregulation upon loss of H2BE. Next, we compared RNA-seq data to ATAC-seq data to determine the
204 relationship between changes in accessibility and gene expression. This analysis revealed that ~60% of
205 downregulated genes show decreased accessibility at the transcription start site and/or proximal enhancers for

206 that gene (Fig 4d). Further, genes downregulated in KO showed the greatest decrease in accessibility by ATAC-
207 seq (Fig 4e). Taken together, these data suggest that downregulated genes are the most highly expressed in WT
208 and show the greatest changes in accessibility. Downregulated genes that did not overlap with ATAC peaks, as
209 well as upregulated genes may be due to secondary or compensatory mechanisms or other yet unknown
210 functions of H2BE. Finally, overlap of CUT&Tag, ATAC, and RNA sequencing datasets identified genes with H2BE
211 enrichment in WT neurons, changes in chromatin compaction in KO, and decreased transcription in KO,
212 including *Slc8a2 and Tuba1a* (Fig 4f; Supp Fig 4b-e).

213 **H2BE affects neuronal gene expression in the brain**

214 We next wanted to understand the function of H2BE in the brain. Given that H2BE is expressed at negligible
215 levels early in life, we predicted H2BE loss would not have substantial effects on cell identity. Rather we
216 predicted it may affect gene expression within cell types as a consequence of the cumulative effects of H2BE
217 loss into adulthood. We therefore performed single-nucleus Drop-seq[40] on cortical tissue from adult WT and KO
218 mice. We identified 20 unique cell clusters, including 10 excitatory neuron clusters, 5 inhibitory neurons, one
219 cluster of claustrum neurons, and 4 non-neuronal subtypes (Fig 5a). We did not detect notable changes in cluster
220 identity across genotypes (Fig 5b, Supp Fig 5a), providing additional evidence that the effect of H2BE
221 accumulates after development. Neuronal clusters were annotated according to the cortical layer they occupy,
222 or—if unidentifiable by cortical layer—according to the gene most differentially expressed in that cluster relative
223 to all other excitatory or inhibitory neuronal clusters. We identified differentially expressed genes in almost all
224 neuronal clusters (Fig 5c; Supp Fig 5b), and also in non-neuronal cells, including astrocytes, oligodendrocytes,
225 and microglia (Supp Fig 5b).

226 Of all excitatory neurons, the two clusters from cortical layer 2/3 had the most differential gene expression.
227 Looking at the excitatory cluster with the greatest number of downregulated genes, from layer 2/3 pyramidal
228 neurons (Ex_L2/3_2), we observed substantially more downregulated genes (114) than upregulated (21) which
229 was true of most cell types (Fig 5d; Supp Fig 5c). These downregulated genes are involved in synaptic functions

230 such as cell-cell adhesion (*Nlgn1, Nrxn1*), pre- and postsynaptic membrane assembly (*Il1rapl1, Magi2*), and
231 trans-synaptic signaling (*Grm7, Tenm2*) (Fig 5e). We next overlapped the down- and upregulated genes from
232 the top 5 excitatory clusters, identifying 14 downregulated genes and 7 upregulated genes in common (Fig 5f-
233 g; Supp Fig 5c). The inhibitory cluster with the most differentially expressed genes, inhibitory cluster with
234 Phactr1 expression (Inh_Phactr1), included 284 down- and 18 upregulated genes (Fig 5h). Gene ontology
235 analysis of these genes reveals similar annotations to those from layer 2/3 pyramidal neurons (Ex_L2/3_2),
236 though with lower enrichment scores (Fig 5i). We overlapped the differential gene lists from the top 3 inhibitory
237 clusters and identified 12 downregulated and 2 upregulated genes in common between these clusters (Fig 5j-k;
238 Supp Fig 5d). Notably, there are 6 downregulated genes and 2 upregulated genes found in all top excitatory and
239 inhibitory clusters shown here, indicating a pronounced role for H2BE in the expression of these genes across
240 all neuronal cell types. In summary, H2BE is essential for the expression of synaptic genes in the adult mouse
241 brain with similar disruptions to genes that regulate synaptic function observed across multiple cell types.

242 **H2BE regulates synaptic strength and is required for long-term memory**

243 These intersecting changes in synaptic gene expression raise the possibility that knocking out H2BE will lead to
244 weakened or otherwise impaired synapses. To assess synaptic function, we performed field recordings of
245 pharmacologically isolated excitatory postsynaptic potentials (fEPSP) from the stratum radiatum of the CA1
246 region in acute hippocampal slices. We electrically stimulated Schaffer collateral fibers with increasing input
247 voltage, observing that the slope of the resulting fEPSP increases in both WT and KO. However, the response is
248 significantly lower in KO, suggesting that synapses are weaker in KO in response to the same intensity stimulus
249 (Fig 6a). To rule out that these differences in synaptic strength resulted from altered recruitment of Schaffer
250 collaterals, we also measured fiber volley amplitude in response to the same stimuli and saw no difference
251 between WT and KO (Fig 6b-c). Together, these data suggest that excitatory glutamatergic synaptic transmission
252 is weakened in KO neurons supporting our finding that H2BE promotes the expression of synaptic genes.

253 Alterations in synaptic function can cause deficits in cognition. Therefore, we performed a battery of behavioral
254 assays to analyze the role of H2BE in cognition and learning using an H2BE-KO mouse. First, we assessed
255 olfactory function due to the high level of H2BE expression in the mouse olfactory tissues[29]. Previous work found
256 that H2BE KO caused a deficit in olfactory discrimination in a learning paradigm. However, based on findings
257 that H2BE is expressed throughout the brain (Fig. 1b, Supp Fig1f-h), it is unclear if these deficits are due to
258 olfactory dysfunction or indicative of broader learning and memory deficits. We therefore first performed a test
259 of olfactory habituation and dishabituation[41] through repeated exposure to the same odorant followed by
260 exposure to novel odorants. Mice are expected to show less interest in odors after repeated presentations and
261 increased interest when new odors are introduced. We found that KO mice have intact habituation and
262 dishabituation to a variety of non-social and social olfactory cues (Fig 6d). There is a significant effect of sex on
263 time spent interacting with the olfactory cues, with females showing greater interaction time with odor cues.
264 However, within sex there was no effect of genotype on interaction with any of the cues (Supp Fig 6a). This
265 behavior serves as an important control behavior and suggests intact olfactory processing. Regardless, in all
266 tests (except for sociability measures) we removed all odor cues to remove potential confounds in the case that
267 subtle deficits were not detected. Notably, these findings fit with published data demonstrating that KOs have
268 intact odor evoked electrical responses in the olfactory epithelium[29] but raise the possibility that deficits may
269 be due to other cognitive disruptions. In an open field arena, WT and KO mice traveled the same distance when
270 allowed to explore freely, though there was an overall effect of sex, with male mice traveling a shorter distance
271 during the trial compared to female mice (Fig 6e; Supp Fig 6b). There was no effect of H2BE KO on anxiety-like
272 behavior as assessed by time spent in the center zone of an open field arena (Supp Fig 6c). These behavioral
273 tests indicate KO mice have intact olfaction and no detectable mobility deficits or changes in anxiety and
274 exploratory behaviors.

275 Due to the well-documented role of synaptic genes in social behaviors[42–44], we tested the sociability of WT and
276 KO mice. Mice were placed in a three-chamber apparatus containing a rock or mouse in each of the outer

277 chambers and a neutral center chamber. Mice were allowed to explore freely, and we measured the amount of
278 time spent interacting with the mouse and rock. A discrimination index was calculated for each mouse by finding
279 the difference between interaction time with the mouse and rock as a proportion of total time spent interacting
280 with the two. Both WT and KO mice show a preference for the mouse (as measured by a positive discrimination
281 index) (Fig 6f). However, subtle changes were detected in average interaction duration with the mouse observed
282 (Supp Fig 6d-f) suggesting largely intact sociability with minor changes in social behavior.

283 We next tested KO mice and control littermates in a T-maze to test working memory. In the T-maze, mice were
284 placed at the entrance to a T-shaped maze and allowed to explore freely. Mice with intact working memory and
285 normal exploratory behavior typically alternate between the three arms before returning to the first arm visited.
286 WT and KO mice exhibited similar rates of 3-arm alternations with no effect of sex (Fig 6g), suggesting that
287 exploratory behavior and working memory remain intact in KO mice.

288 Finally, we tested long-term memory in mice, specifically selecting tests that rely on proper synapse
289 regulation[45–47]. In a novel object recognition test, mice are exposed to two identical objects in an arena and
290 allowed to explore freely. On the following day, one of the objects is replaced with a novel object, and mice are
291 returned to the arena. Due to a natural preference for novelty, mice that recognize the familiar object during
292 testing spend more time exploring the novel object than the familiar object. We observed that mice lacking
293 H2BE were not able to distinguish between a novel object and a familiar object presented 24 hours earlier with
294 no effect of sex (Fig. 6h), suggesting that long-term memory is disrupted in KO mice. Importantly, there were no
295 differences between groups in total time spent with both objects during learning or testing (Supp Fig 6g-h),
296 indicating that deficits were not due to differences in object exploration.

297 We also assessed mice in two complementary tests of long-term memory—cued and contextual fear
298 conditioning. In these assays, mice are exposed to two foot-shocks paired with a tone cue. For recall, mice are
299 placed back in the chamber and freezing behavior is quantified as a readout of fear memory. In contextual

300 conditioning trials, mice are returned to the chamber or "context" 24 hours or 14 days post-training and freezing
301 behavior is measured. For cued conditioning trials, mice are placed in an altered context and re-exposed to the
302 tone cue alone (no foot-shock) 48 hours or 15 days post-training and freezing is measured during the tone
303 presentations. In both cued and contextual recall, there was no effect of sex. However, KO mice exhibit less
304 freezing behavior 14 (or 15) days post-training compared to their control littermates (Fig 6i-j). There was no
305 difference in freezing behavior prior to the initial tone-shock pair ("Pre-shock") or in response to the first tone
306 presentation ("Tone 1"), illustrating that there was nothing inherently fearful about the context or tone cue
307 alone. Interestingly, in both contextual and cued conditioning, knockout mice showed a trend toward decreased
308 freezing at 24 hour (contextual) or 48 hour (cued) post-training, however this difference did not reach
309 significance. Together, these results demonstrate a critical role for H2BE in long-term memory, while olfaction,
310 motor behavior, exploration, social behavior, and working memory are largely spared.

311 In summary, these findings support an overarching model in which H2BE promotes accessibility at critical and
312 highly expressed neuronal genes to support synaptic responses and robust memory. Thus, when H2BE is lost,
313 chromatin adopts a more closed state and synaptic gene expression is reduced, leading to synaptic dysfunction
314 and impaired long-term memory (Fig 7).

315 **DISCUSSION**

316 Here, we show widespread expression of H2BE throughout the brain, with specific enrichment at gene
317 promoters. The expression of H2BE results in greater chromatin accessibility which is reliant on a single amino
318 acid that lies at the interface between the histone octamer and nucleosomal DNA. Further, we show that loss
319 of H2BE results in broad changes in gene expression in both primary neuronal cultures and in neurons derived
320 from the adult brain. Lastly, we show that H2BE is critical for long-term memory. In summary, we provide
321 evidence of a novel example of how histone variants in the brain are critical to controlling chromatin structure,
322 transcription, and memory.

323

324 The five amino acids that differ between H2BE and canonical H2B are distributed across the length of the protein
325 rather than clustered together. This provides a unique opportunity to link a single amino acid site to the distinct
326 properties of H2BE and sets H2BE apart from other better understood histone variants[48,49]. We found that one
327 of these amino acids, I39, is critical for the effect of H2BE on chromatin. This places H2BE as a novel example of
328 cases in which a single amino acid on a histone protein is linked to large-scale changes in chromatin regulation.
329 This has recently been shown in two other variants, H2A.Z and H3.3, where a single amino acid is linked to
330 neurological function and the onset of neurodevelopmental disorders[9,26]. Additionally, emerging research on
331 oncohistones has revealed how single amino acid mutations in histone variants cause genome-wide changes
332 that underlie various cancers[50–53]. Our work adds to this emerging theme in chromatin biology and provides a
333 novel example of a variant-specific amino acid that mediates robust changes in chromatin structure.

334

335 This study expands upon previous work linking H2BE expression levels in olfactory tissues to olfactory neuron
336 longevity[29]. In accordance with this study, we see substantial enrichment of H2BE in the mouse main olfactory
337 epithelium (Supp Fig 1i). However, the development of an H2BE-specific antibody, H2BE nucleosomes, and
338 chromatin arrays, along with the expansion of next-generation sequencing technologies has allowed us to define
339 H2BE expression throughout the brain and its function in chromatin regulation. We found no overt deficits in
340 basic olfactory function, consistent with previous results from electro-olfactograms showing no change in
341 electrical responses to odor presentations in the olfactory epithelium of H2BE KO mice[29]. We therefore
342 expanded on the behavioral characterization of H2BE KO mice, showing that long-term memory is impaired in
343 KO mice, while other important behaviors such as motor function, exploratory behavior, social behavior, and
344 working memory remain intact. Notably, none of our findings disagree with previous work but use newly
345 available tools to provide an in-depth analysis of H2BE expression and function.

346

347 With the finding that H2BE is expressed throughout the brain, several questions remain outstanding regarding
348 the mechanism of H2BE expression and its function. We've shown that H2BE expression is enriched at
349 promoters, yet the mechanism by which this enrichment occurs remains unknown. One possibility is that this
350 expression pattern is mediated by chaperone proteins that specifically deposit H2BE at promoters. Alternatively,
351 greater histone turnover at regions of open chromatin may result in the accumulation of H2BE at those sites
352 which then serves to maintain accessible chromatin states. Further, while we observe large-scale changes in
353 transcription upon knocking out H2BE, only a subset of downregulated genes (~60%) can be explained by a loss
354 of accessibility. Further study is required to explain the remaining 40% of downregulated genes and the genes
355 that are upregulated upon loss of H2BE. We speculate that some of these differential gene expression patterns
356 may be explained by secondary or compensatory mechanisms, or by functions of H2BE that have not yet been
357 discovered. We also found that H2BE is expressed in other cell types other than neurons in the brain. H2BE KO
358 mice have no overt health issues or disruptions in basic motor and cognitive functions, suggesting that the
359 memory deficits that we observed are not due to major health issues. However, it is plausible that H2BE has
360 distinct roles in other cell types. Further, the role of H2BE in other cell types in the brain or other systems could
361 emerge in other biological contexts, including disease, aging, or other perturbations.
362
363 Lastly, there is a growing body of clinical data linking histone variants to neurological disorders. To date H2BE
364 has not been linked to neurological or neurodevelopmental disorders. However, a recent study of human
365 histone genes suggests that H2BE is intolerant to mutations, suggesting that mutations in H2BE may be
366 pathogenic[54]. We anticipate that with increased use of whole exome sequencing in patients with unexplained
367 neurodevelopmental disorders, it is likely that future work will reveal mutations within H2BE, similar to
368 disorders recently linked to other histone variant proteins[9,10]. In summary, this work reveals how histone variant
369 H2BE contributes to the complex chromatin environment in the brain. This research furthers our understanding
370 of mechanisms by which neurons control transcription and ultimately govern behavior. Further, this work

371 provides insight into novel mechanisms underlying memory and the increasing number of neurodevelopmental

372 disorders linked to disruptions in chromatin regulation.

373 **Acknowledgements:** We thank Drs. Catherine Dulac and Stephen Santoro for sharing reagents and mouse lines.
374 Mass spectrometry was performed with the CHOP-Penn Proteomics Core. Behavior procedures were performed
375 with the Neurobehavior Testing Core at University of Pennsylvania. We acknowledge the use of the MSK
376 Molecular Cytology Core Facility, supported by the NCI Cancer Center Support Grant (CCSG, P30 CA08748), Cycle
377 for Survival, and the Marie-Josée and Henry R. Kravis Center for Molecular Oncology. E.H. is supported by NIH
378 grant F31MH126576. S.L, K.P., and E.K., were supported by NIH grants 1DP2MH129985 and R00MH111836 and
379 by the Klingenstein-Simons Fellowship from the Esther A. & Joseph Klingenstein Fund and the Simons
380 Foundation, the Alfred P. Sloan Foundation Research Fellowship (FG-2020-13529), the Brain and Behavior
381 Research Foundation NARSAD Young Investigator Award, and pilot funding from the Epigenetics Institute at the
382 University of Pennsylvania. N.A.P. is supported by NIH grant F99CA264420.

383 **Competing interest statement:** The authors have no conflicts of interest.

384 **REFERENCES**

385

386 1. Borrelli, E., Nestler, E. J., Allis, C. D. & Sassone-Corsi, P. Decoding the Epigenetic Language of Neuronal
387 Plasticity. *Neuron* **60**, 961–974 (2008).
388 2. Gallegos, D. A., Chan, U., Chen, L.-F. & West, A. E. Chromatin Regulation of Neuronal Maturation and
389 Plasticity. *Trends Neurosci* **41**, 311–324 (2018).
390 3. Zovkic, I. B. Epigenetics and memory: an expanded role for chromatin dynamics. *Current Opinion in*
391 *Neurobiology* **67**, 58–65 (2021).
392 4. Iossifov, I. *et al.* The contribution of de novo coding mutations to autism spectrum disorder. *Nature*
393 **515**, 216–221 (2014).
394 5. Parikshak, N. N. *et al.* Integrative Functional Genomic Analyses Implicate Specific Molecular Pathways
395 and Circuits in Autism. *Cell* **155**, 1008–1021 (2013).
396 6. O'Roak, B. J. *et al.* Sporadic autism exomes reveal a highly interconnected protein network of de novo
397 mutations. *Nature* **485**, 246–250 (2012).
398 7. Iossifov, I. *et al.* De Novo Gene Disruptions in Children on the Autistic Spectrum. *Neuron* **74**, 285–299
399 (2012).
400 8. Thudium, S., Palozola, K., L'Her, É. & Korb, E. Identification of a transcriptional signature found in
401 multiple models of ASD and related disorders. *Genome Res.* **32**, 1642–1654 (2022).
402 9. Greenberg, R. S., Long, H. K., Swigut, T. & Wysocka, J. Single Amino Acid Change Underlies Distinct
403 Roles of H2A.Z Subtypes in Human Syndrome. *Cell* **178**, 1421-1436.e24 (2019).
404 10. Bryant, L. *et al.* Histone H3.3 beyond cancer: Germline mutations in *Histone 3 Family 3A and 3B* cause a
405 previously unidentified neurodegenerative disorder in 46 patients. *Sci. Adv.* **6**, eabc9207 (2020).
406 11. Berson, A., Nativio, R., Berger, S. L. & Bonini, N. M. Epigenetic Regulation in Neurodegenerative
407 Diseases. *Trends Neurosci* **41**, 587–598 (2018).

408 12. Nativio, R. *et al.* An integrated multi-omics approach identifies epigenetic alterations associated with
409 Alzheimer's disease. *Nat Genet* **52**, 1024–1035 (2020).
410 13. Nativio, R. *et al.* Dysregulation of the epigenetic landscape of normal aging in Alzheimer's disease. *Nat*
411 *Neurosci* **21**, 497–505 (2018).
412 14. Luger, K., Mäder, A. W., Richmond, R. K., Sargent, D. F. & Richmond, T. J. Crystal structure of the
413 nucleosome core particle at 2.8 Å resolution. *Nature* **389**, 251–260 (1997).
414 15. Martire, S. & Banaszynski, L. A. The roles of histone variants in fine-tuning chromatin organization and
415 function. *Nat Rev Mol Cell Biol* **21**, 522–541 (2020).
416 16. Marzluff, W. F., Wagner, E. J. & Duronio, R. J. Metabolism and regulation of canonical histone mRNAs:
417 life without a poly(A) tail. *Nat Rev Genet* **9**, 843–854 (2008).
418 17. Marzluff, W. F., Gongidi, P., Woods, K. R., Jin, J. & Maltais, L. J. The human and mouse replication-
419 dependent histone genes. *Genomics* **80**, 487–498 (2002).
420 18. Talbert, P. B. & Henikoff, S. Histone variants — ancient wrap artists of the epigenome. *Nat Rev Mol Cell*
421 *Biol* **11**, 264–275 (2010).
422 19. Maze, I. *et al.* Critical Role of Histone Turnover in Neuronal Transcription and Plasticity. *Neuron* **87**, 77–
423 94 (2015).
424 20. Zovkic, I. B., Paulukaitis, B. S., Day, J. J., Etikala, D. M. & Sweatt, J. D. Histone H2A.Z subunit exchange
425 controls consolidation of recent and remote memory. *Nature* **515**, 582–586 (2014).
426 21. Yang, Y. *et al.* Chromatin remodeling inactivates activity genes and regulates neural coding. *Science*
427 **353**, 300–305 (2016).
428 22. Stefanelli, G. *et al.* Learning and Age-Related Changes in Genome-wide H2A.Z Binding in the Mouse
429 Hippocampus. *Cell Rep* **22**, 1124–1131 (2018).
430 23. Lepack, A. E. *et al.* Aberrant H3.3 dynamics in NAc promote vulnerability to depressive-like behavior.
431 *Proc. Natl. Acad. Sci. U.S.A.* **113**, 12562–12567 (2016).

432 24. Narkaj, K. *et al.* Blocking H2A.Z Incorporation via Tip60 Inhibition Promotes Systems Consolidation of
433 Fear Memory in Mice. *eNeuro* **5**, (2018).
434 25. Dunn, C. J. *et al.* Histone Hypervariants H2A.Z.1 and H2A.Z.2 Play Independent and Context-Specific
435 Roles in Neuronal Activity-Induced Transcription of *Arc/Arg3.1* and Other Immediate Early Genes. *eNeuro* **4**,
436 ENEURO.0040-17.2017 (2017).
437 26. Khazaei, S. *et al.* Single substitution in H3.3G34 alters DNMT3A recruitment to cause progressive
438 neurodegeneration. *Cell* **186**, 1162-1178.e20 (2023).
439 27. Wimmer, M. E. *et al.* H3.3 Barcoding of Nucleus Accumbens Transcriptional Activity Identifies Novel
440 Molecular Cascades Associated with Cocaine Self-administration in Mice. *J. Neurosci.* **39**, 5247–5254 (2019).
441 28. Raman, P. *et al.* Novel Classes and Evolutionary Turnover of Histone H2B Variants in the Mammalian
442 Germline. *Mol Biol Evol* **39**, msac019 (2022).
443 29. Santoro, S. W. & Dulac, C. The activity-dependent histone variant H2BE modulates the life span of
444 olfactory neurons. *eLife* **1**, e00070 (2012).
445 30. Gamble, M. J., Frizzell, K. M., Yang, C., Krishnakumar, R. & Kraus, W. L. The histone variant macroH2A1
446 marks repressed autosomal chromatin, but protects a subset of its target genes from silencing. *Genes Dev* **24**,
447 21–32 (2010).
448 31. Sun, Z. *et al.* Transcription-associated histone pruning demarcates macroH2A chromatin domains. *Nat*
449 *Struct Mol Biol* **25**, 958–970 (2018).
450 32. Seo, J. *et al.* Genome-wide profiles of H2AX and γ-H2AX differentiate endogenous and exogenous DNA
451 damage hotspots in human cells. *Nucleic Acids Res* **40**, 5965–5974 (2012).
452 33. Palmer, D. K., O'Day, K., Trong, H. L., Charbonneau, H. & Margolis, R. L. Purification of the centromere-
453 specific protein CENP-A and demonstration that it is a distinctive histone. *Proc. Natl. Acad. Sci. U.S.A.* **88**,
454 3734–3738 (1991).
455 34. Kaya-Okur, H. S. *et al.* CUT&Tag for efficient epigenomic profiling of small samples and single cells. *Nat*
456 *Commun* **10**, 1930 (2019).

457 35. Krzemien, K. M., Beckers, M., Quack, S. & Michaelis, J. Atomic force microscopy of chromatin arrays
458 reveal non-monotonic salt dependence of array compaction in solution. *PLoS ONE* **12**, e0173459 (2017).
459 36. Schwarz, P. M., Felthauser, A., Fletcher, T. M. & Hansen, J. C. Reversible Oligonucleosome Self-
460 Association: Dependence on Divalent Cations and Core Histone Tail Domains. *Biochemistry* **35**, 4009–4015
461 (1996).
462 37. Buenrostro, J. D., Wu, B., Chang, H. Y. & Greenleaf, W. J. ATAC-seq: A Method for Assaying Chromatin
463 Accessibility Genome-Wide. *Current Protocols in Molecular Biology* **109**, (2015).
464 38. Arimura, Y. *et al.* Cancer-associated mutations of histones H2B, H3.1 and H2A.Z.1 affect the structure
465 and stability of the nucleosome. *Nucleic Acids Res* **46**, 10007–10018 (2018).
466 39. Koopmans, F. *et al.* SynGO: An Evidence-Based, Expert-Curated Knowledge Base for the Synapse.
467 *Neuron* **103**, 217-234.e4 (2019).
468 40. Hu, P. *et al.* Dissecting Cell-Type Composition and Activity-Dependent Transcriptional State in
469 Mammalian Brains by Massively Parallel Single-Nucleus RNA-Seq. *Molecular Cell* **68**, 1006-1015.e7 (2017).
470 41. Yang, M. & Crawley, J. N. Simple Behavioral Assessment of Mouse Olfaction. *CP Neuroscience* **48**,
471 (2009).
472 42. Spratt, P. W. E. *et al.* The Autism-Associated Gene Scn2a Contributes to Dendritic Excitability and
473 Synaptic Function in the Prefrontal Cortex. *Neuron* **103**, 673-685.e5 (2019).
474 43. Yan, Y. *et al.* ASH1L haploinsufficiency results in autistic-like phenotypes in mice and links Eph receptor
475 gene to autism spectrum disorder. *Neuron* **110**, 1156-1172.e9 (2022).
476 44. O'Connor, E. C., Bariselli, S. & Bellone, C. Synaptic basis of social dysfunction: a focus on postsynaptic
477 proteins linking group- I m G lu R s with AMPAR s and NMDAR s. *Eur J of Neuroscience* **39**, 1114–1129 (2014).
478 45. Clarke, J. R., Cammarota, M., Gruart, A., Izquierdo, I. & Delgado-García, J. M. Plastic modifications
479 induced by object recognition memory processing. *Proc. Natl. Acad. Sci. U.S.A.* **107**, 2652–2657 (2010).
480 46. Choi, D. I. *et al.* Synaptic correlates of associative fear memory in the lateral amygdala. *Neuron* **109**,
481 2717-2726.e3 (2021).

482 47. Sheynikhovich, D., Otani, S., Bai, J. & Arleo, A. Long-term memory, synaptic plasticity and dopamine in
483 rodent medial prefrontal cortex: Role in executive functions. *Front. Behav. Neurosci.* **16**, 1068271 (2023).
484 48. Hake, S. B. & Allis, C. D. Histone H3 variants and their potential role in indexing mammalian genomes:
485 the 'H3 barcode hypothesis'. *Proc Natl Acad Sci U S A* **103**, 6428–6435 (2006).
486 49. Giaimo, B. D., Ferrante, F., Herchenröther, A., Hake, S. B. & Borggrefe, T. The histone variant H2A.Z in
487 gene regulation. *Epigenetics & Chromatin* **12**, 37 (2019).
488 50. Nacev, B. A. *et al.* The expanding landscape of 'oncohistone' mutations in human cancers. *Nature* **567**,
489 473–478 (2019).
490 51. Bagert, J. D. *et al.* Oncohistone mutations enhance chromatin remodeling and alter cell fates. *Nat*
491 *Chem Biol* **17**, 403–411 (2021).
492 52. Lewis, P. W. *et al.* Inhibition of PRC2 Activity by a Gain-of-Function H3 Mutation Found in Pediatric
493 Glioblastoma. *Science* **340**, 857–861 (2013).
494 53. Stafford, J. M. *et al.* Multiple modes of PRC2 inhibition elicit global chromatin alterations in H3K27M
495 pediatric glioma. *Sci. Adv.* **4**, eaau5935 (2018).
496 54. Lubin, E., Bryant, L., Aicher, J., Li, D. & Bhoj, E. Analysis of histone variant constraint and tissue
497 expression suggests five potential novel human disease genes: H2AFY2, H2AFZ, H2AFY, H2AFV, H1F0. *Hum*
498 *Genet* **141**, 1409–1421 (2022).
499

500

501 **FIGURE LEGENDS**

502 **Figure 1. H2BE is expressed at promoters in neurons.** (a) H2B and H2BE amino acid sequence. Variant amino
503 acids are highlighted in red. (b) Representative western blot for H2BE and H2B in brain tissue from 3–5-month-
504 old WT and KO mice (ctx = cortex; hpc = hippocampus; crb = cerebellum). H2B serves as loading control. (c)
505 Representative immunofluorescent images of cortical tissue from 3-month-old mice stained with H2BE,
506 neuronal marker NeuN, and nuclear marker DAPI. Scale bar = 20µm. (d) LC/MS-MS quantification of H2BE in
507 cortical tissue across age (n = 6-10 biological replicates per age with 3-5 from both male and female combined;
508 data represents mean +/- SEM; one-way ANOVA with Dunnett's multiple comparisons test; ***p<.001,
509 ****p<.0001). No difference was found between male and female mice. (e) Metaplot of H2BE CUT&Tag profiling
510 in WT primary cortical neurons. Plot shows read counts per million mapped reads (RPM) between the
511 transcription start site (TSS) and transcription end site (TES) +/- 2kb (n = 3 biological replicates per genotype).
512 (f) Genomic distribution of H2BE enrichment sites relative to the entire mouse genome (Chi-square test; *p<.05,
513 ***p<.001). (g) Distribution of H2BE enrichment sites (top) and the entire genome binned by 500bp (bottom)
514 relative to the nearest TSS. (h) Metaplot comparison of H2BE CUT&Tag at genes according to expression level.
515 "Not expressed" was defined as genes with average normalized read counts <3 by RNA-sequencing (n = 8,150
516 genes). Remaining genes were binned into three equally sized groups by average normalized read counts (n =
517 6,028 genes per group). KO shows average across all genes regardless of expression. Plot shows read counts per
518 million mapped reads (RPM) around the transcription start site (TSS) +/- 2kb. (n = 3 biological replicates per
519 genotype). (i) H2BE CUT&Tag peak scores assigned by MACS3 by expression level as defined above (one-way
520 ANOVA with post-hoc pairwise t-tests with Bonferroni correction; ****p<.0001, n.s. = not significant). (j-k) RNA-
521 sequencing (top) and CUT&Tag (bottom) gene tracks for representative mid-expressed (*Ankrd27*) and low-
522 expressed (*E2f7*) genes.

523 **Figure 2. H2BE promotes open chromatin.** (a) Thermal stability assay of H2B- and H2BE-containing nucleosomes
524 yields two melting peaks (Tm) corresponding to dimer and tetramer dissociation, respectively (n=3 biological

525 replicates per group; Welch's t-tests with Holm-Šídák correction). (b) Representative micrographs of H2B- or
526 H2BE-containing nucleosome arrays. Scale bar = 100µm. (c) Volume/surface area quantification of compaction
527 from atomic force microscopy of H2B or H2BE nucleosome arrays (n = 60 H2B arrays, 40 H2BE arrays; Welch's
528 t-test; ****p<.0001). Surface area = Total # of pixels occupied by array. Volume = Total pixel intensity of array.
529 (d) Heat map and (e) metaplot comparison of ATAC-seq average signal from WT and KO primary cortical neurons
530 at all WT peaks. Plot shows read counts per million mapped reads (RPM) at all measured peaks +/- 1kb (n = 3
531 WT biological replicates, 4 KO biological replicates). (f) Normalized ATAC-seq read counts at all ATAC peak sites
532 detected in WT neurons (unpaired t-test; ****p<.0001). (g) Volcano plot showing differential chromatin
533 accessibility between WT and KO at WT ATAC peaks. Blue = peaks that decrease in KO; red = peaks that increase
534 in KO; gray = peaks below significance cut-off of FDR<.05. (h) Heat map and (i) metaplot comparison of ATAC-
535 seq average signal from WT and KO primary cortical neurons at all H2BE binding sites identified by CUT&Tag.
536 Plot shows read counts per million mapped reads (RPM) at all measured peaks +/- 1kb (n = 3 WT biological
537 replicates, 4 KO biological replicates). (j) Normalized ATAC-seq read counts at H2BE binding sites (unpaired t-
538 test; ****p<.0001) (k) Volcano plot showing differential chromatin accessibility at H2BE binding sites. Blue =
539 peaks that decrease in KO; red = peaks that increase in KO; gray = peaks below significance cut-off of FDR<.05.
540 (l) Correlation between H2BE reads in WT neurons and changes in ATAC-seq signal between WT and KO
541 (Spearman correlation; $\rho = 0.74$; $p < 2.2\times10^{-16}$). (m-n) ATAC-seq gene tracks for representative mid-expressed
542 (*Ankrd27*) and low-expressed (*E2f7*) genes.

543 **Figure 3. Single amino acid at the histone-DNA interface drives H2BE effect on chromatin.** (a) Nucleosome
544 surrounded by DNA shows that the H2BE-specific amino acid at site 39 lies at the histone-DNA binding interface.
545 Cyan=H2B; red=V39; white=H2A/H3/H4. (b) Schematic of canonical H2B, WT H2BE, and mutant H2BE
546 sequences. (c) Thermal stability assay of H2BE and H2BE-I39V nucleosomes (n = 3 biological replicates per group;
547 2-way ANOVA). (d) Mg^{2+} precipitation assay of chromatin arrays containing WT H2BE or H2BE-I39V (n=4 per
548 group) (e) Mg^{2+} precipitation assay of chromatin arrays containing canonical H2B or H2B-V39I (n=8 per group)

549 (f) ATAC-seq average signal at all genes (n = 3-8 biological replicates per condition). Plot shows read counts per
550 million mapped reads (RPM) around the transcription start site (TSS) +/- 2kb. (g) ATAC-seq gene tracks for
551 *Ankrd27*.

552 **Figure 4. H2BE promotes synaptic gene expression.** (a) Volcano plot showing differentially expressed genes
553 (FDR<.05, absolute fold change > 1.25) between WT and KO primary cortical neurons (n = 4 biological replicates
554 per genotype [2 male, 2 female]). Blue = downregulated; red = upregulated. (b) Gene ontology enrichment
555 analysis of down- (left) and upregulated (right) genes. (c) Normalized RNA-seq read counts in WT neurons for
556 genes downregulated, upregulated or unchanged in KO (one-way ANOVA with post-hoc pairwise t-tests with
557 Bonferroni correction; ****p<.0001, n.s. = not significant; DEG = differentially expressed genes). (d) Pie chart
558 showing which downregulated genes have a decreased ATAC-seq peak in KO at a proximal enhancer and/or
559 promoter for that gene in WT. (e) ATAC-seq fold change (KO/WT) for downregulated, upregulated, and
560 unchanged genes in KO (one-way ANOVA with post-hoc pairwise t-tests with Bonferroni correction;
561 ****p<.0001, n.s. = not significant; DEG = differentially expressed genes). (f) CUT&Tag, ATAC-seq, and RNA-seq
562 genome browser tracks at the *Slc8a2* locus in WT and KO cortical neurons. See Supplemental Figure 4 for
563 additional example tracks.

564 **Figure 5. H2BE is required for appropriate synaptic function in the brain.** (a) UMAP of single-nucleus
565 transcriptomic profiles from adult (2-4 months) mouse cortices (n = 3 biological replicates per genotype). Colors
566 represent cluster identity. Ex = excitatory neurons; Inh = inhibitory neurons. (b) UMAP clustering with dots
567 representing each nucleus colored by genotype. Relative distribution of WT and KO cells found by cluster shown
568 in Supplemental Figure 5. (c) Number of differentially expressed genes within each cluster for all excitatory and
569 inhibitory neuronal clusters. (d) Volcano plot showing differential expression from WT and KO in a
570 representative cluster of layer 2/3 cortical excitatory neurons (Ex_L2/3_2). Blue = downregulated; red =
571 upregulated. (e) Gene ontology enrichment analysis of downregulated genes in cluster Ex_L2/3_2. Upregulated
572 shown in Supplemental Figure 5. (f-g) Overlap of differentially expressed down- (f) and upregulated (g) genes

573 from the 5 excitatory neuron clusters with the greatest number of differentially expressed genes. (h) Volcano
574 plot showing differential expression from WT and KO cortical inhibitory neurons in a representative cluster,
575 Inh_Phactr1. Blue = downregulated; red = upregulated. (i) Gene ontology enrichment analysis of downregulated
576 genes in cluster Inh_Phactr1. (j-k) Overlap of differentially expressed down- (j) and upregulated (k) genes from
577 the 3 inhibitory neuron clusters with the greatest number of differently expressed genes.

578 **Figure 6. H2BE is required for long-term memory.** (a) Input-output curves from field extracellular postsynaptic
579 potentials and (b) afferent fiber volleys following stimulation of hippocampal Schaffer collaterals. The line
580 represents the inferred responses through linear regression (WT r^2=0.6748, KO r^2=0.5006), while each dot
581 corresponds to the averaged slope from each experiment based on stimulus intensity. (n = 11/13 from 5/4
582 animals [2-3 males and females per genotype]; two-way ANOVA [stimulus intensity x genotype] with Šídák's
583 multiple comparisons test; *p<.05, **p<.01, ***p<.001). (c) Representative traces from WT and KO. (d)
584 Interaction time with a scented cotton swab during presentations of water, two non-social odors (almond,
585 vanilla), and social odors (same sex, opposite sex) for three consecutive trials per scent. Line and shaded area
586 represent mean +/- SEM (n = 20 WT mice [8 male, 12 female], 24 KO mice [10 male, 14 female]; two-way ANOVA
587 [genotype x sex] for each odorant. No differences were detected between genotypes. Significant differences
588 were detected between sex (graphed separately in Supplemental Figure 6a). (e) Distance traveled in an open
589 field arena during a 5-minute trial (n = 19 WT mice [9 male, 10 female], 19 KO mice [11 male, 8 female]; two-
590 way ANOVA [genotype x sex]). Sexes graphed separately in Supplemental Figure 6b. (f) Discrimination index for
591 interaction time between a mouse and a rock during a 3-chamber sociability SEM (n = 20 WT mice [8 male, 12
592 female], 24 KO mice [10 male, 14 female]; two-way ANOVA [genotype x sex]). DI = ([mouse – rock] / [mouse +
593 rock]). No effects of sex were observed. (g) Percent correct trials of spontaneous alternation in a T-maze trial (n
594 = 19 WT mice [9 male, 10 female], 19 KO mice [11 male, 8 female]; two-way ANOVA [genotype x sex]). No effects
595 of sex were observed. (h) Discrimination index during a novel object recognition task (n = 19 WT mice [9 male,
596 10 female], 19 KO mice [11 male, 8 female]; two-way ANOVA [genotype x sex]; *p<.05)]). DI = ([novel – familiar]

597 / [novel + familiar]). No effects of sex were observed. (i-j) Percent freezing during cued (i) and contextual (j) fear
598 conditioning (n = 20 WT mice [8 male, 12 female], 24 KO mice [10 male, 14 female]; two-way ANOVA [genotype
599 x sex] for each phase of testing; **p<.01).

600 **Figure 7. Model of H2BE function.** In a WT mouse, H2BE is expressed at promoters throughout the genome,
601 where its expression causes chromatin to open and higher levels of synaptic gene expressions. This supports
602 healthy synapses and proper neuronal function. In contrast, upon loss of H2BE chromatin remains in a closed
603 state, there is loss of synaptic gene expression, synaptic dysfunction, and impaired long-term memory.

604 **Supplemental Figure 1.** (a) Dot blot analysis of H2BE antibody against N terminal peptides for H2BE, H2B, and
605 H3. (b) Schematic of the H2BE-KO/Gap43-mCherry KI allele as generated by Santoro & Dulac (2012). (c) RNA-
606 sequencing heat map of WT and KO primary cortical neurons at the *H2bc21* locus shows no reads in the H2BE
607 coding sequence in KO neurons. (d) Pie chart of progeny from $H2BE^{+/-}$ x $H2BE^{+/-}$ crosses show expected
608 Mendelian ratios (n = 126 mice from 26 litters). (e) Representative western blot for H2BE and H2B in cortical
609 tissue. WT and KO demonstrates anti-H2BE antibody specificity. H2B serves as loading control. (f)
610 Representative western blot for H2BE and H2B in cortical tissue from WT and KO primary cortical neurons
611 demonstrates anti-H2BE antibody specificity. H2B serves as loading control. (g) Representative
612 immunofluorescent images of cortical tissue from mice stained with H2BE and the nuclear marker DAPI
613 demonstrates anti-H2BE antibody specificity. Scale bar = 30µm. (h) Representative western blot for H2BE and
614 H2B in various tissues from WT and KO mice. (i) Representative MS/MS spectra of the H2B and H2BE peptides.
615 (j) Metaplot comparison of CUT&Tag sequencing average signal from WT and KO primary cortical neurons
616 demonstrates anti-H2BE antibody specificity. Plot shows read counts per million mapped reads (RPM) around
617 the transcription start site (TSS) +/- 2kb (n = 1 biological replicate per genotype). (k) Overlap analysis of H2BE
618 peaks detected by CUT&Tag from 3 biological replicates. (l) Genomic distribution of H2BE peaks detected by
619 CUT&Tag. (m) Gene ontology enrichment analysis of genes where H2BE is enriched.

620 **Supplemental Figure 2.** (a) Volume of H2B or H2BE nucleosome arrays. (n = 60 H2B arrays, 40 H2BE arrays;
621 Welch's t-test). Volume = total pixel intensity of each array. (b) Mg^{2+} precipitation assay for chromatin arrays
622 containing canonical H2B or variant H2BE (n = 4 per group). (c) Metaplot comparison of ATAC-seq average signal
623 from WT and KO primary cortical neurons at all transcription start sites. Plot shows read counts per million
624 mapped reads (RPM) around the transcription start site (TSS) +/- 2kb (n = 3 WT biological replicates, 4 KO
625 biological replicates). (d) Volcano plot showing differential chromatin accessibility between WT and KO at
626 transcription start sites. Blue = peaks that decrease in KO; red = peaks that increase in KO; gray = peaks below
627 significance cut-off of FDR<.05. (e) Normalized ATAC-seq read counts at transcription start sites with significantly
628 different accessibility in WT (left) or KO (right). (unpaired t-test; ****p<.0001). (f) Metaplot comparison of ATAC-
629 seq average signal from WT and KO primary cortical neurons at all enhancers identified in brain tissue. Plot
630 shows read counts per million mapped reads (RPM) at all measured enhancers +/- 1kb (n = 3 WT biological
631 replicates, 4 KO biological replicates). (g) Volcano plot showing differential chromatin accessibility between WT
632 and KO at enhancers. Blue = peaks that decrease in KO; red = peaks that increase in KO; gray = peaks below
633 significance cut-off of FDR<.05. (h) Normalized ATAC-seq read counts at transcription start sites with significantly
634 different accessibility in WT (left) or KO (right). (unpaired t-test; ****p<.0001). (i) Summary plot (top) of peaks
635 with decreased (purple) or increased (blue) accessibility in KO with heatmap (bottom) showing each TSS. The
636 majority of TSS regions show decreased accessibility in KO. (j) Normalized ATAC-seq read counts at all WT ATAC-
637 seq peaks with significantly different accessibility in WT (left) or KO (right). (unpaired t-test; ****p<.0001). (k)
638 Percent of all detected ATAC-seq peaks within H2BE binding sites at promoters, within the gene body, or
639 intergenic that are significantly decreased in KO. (l) Summary plot (top) and heatmap (bottom) of CUT&Tag
640 reads and ATAC-seq reads at all H2BE binding sites, partitioned by genomic region.

641 **Supplemental Figure 3.** (a) Mononucleosome electrophoretic mobility shift assay using native polyacrylamide
642 gel electrophoresis to validate nucleosome assembly, stained using ethidium bromide to visualize DNA. (b)
643 Chromatin array electrophoretic mobility shift assay using native agarose-polyacrylamide gel electrophoresis

644 (APAGE) to validate chromatin array assembly, stained with ethidium bromide. (c) Western blot for H2BE and
645 H2B in protein lysates from WT and KO neurons, and KO neurons infected with viruses expressing WT H2BE,
646 H2BE-I39V, canonical H2B, or a GFP control.

647 **Supplemental Figure 4.** (a) Synaptic gene ontology enrichment analysis by SynGO of genes where H2BE is
648 enriched. (b) Overlap analysis of genes with H2BE enrichment, decreased accessibility in KO, and decreased
649 transcription in KO. (c) CUT&Tag, ATAC-seq, and RNA-seq genome browser tracks at the *Tuba1a* locus in WT and
650 KO cortical neurons. (d-e) RNA-seq tracks from WT and KO primary cortical neurons at (d) *Ankrd27* and (e) *E2f7*
651 previously shown in Figs 1 and 2.

652 **Supplemental Figure 5.** (a) Analysis of the difference between the proportion of WT and KO nuclei in each
653 cluster. Data represents the fold change in WT vs KO nuclei in the cluster and a confidence interval for the
654 magnitude difference. Clusters with fold difference >1.8 and FDR<.05 highlighted in pink. Ex_Angpt1 cluster
655 contains only small number of nuclei with 84 nuclei in WT and 45 in KO. (b) Number of differentially expressed
656 genes within glial clusters and claustral neurons from single-nucleus RNA-seq. (c-d) CUT&Tag, ATAC-seq, and
657 RNA-seq genome browser tracks at the *Tuba1a* locus in WT and KO cortical neurons. Note that these gene
658 ontology analyses produced the same results because of a high concordance between neuronal clusters and by
659 nature of the small gene lists produced by snRNA-seq.

660 **Supplemental Figure 6.** (a) Olfactory habituation/dishabituation data separated by sex. Line and shaded area
661 represent mean +/- SEM (n = 20 WT mice [8 male, 12 female], 24 KO mice [10 male, 14 female]). (b) Distance
662 traveled in an open field arena during a 5-minute trial separated by sex (n = 19 WT mice [9 male, 10 female], 19
663 KO mice [11 male, 8 female]; two-way ANOVA [genotype x sex]; main effect of sex; ***p<.001). (c) Time spent
664 in center zone of an open field arena during a 5-minute trial sex (n = 19 WT mice [9 male, 10 female], 19 KO
665 mice [11 male, 8 female]; two-way ANOVA [genotype x sex]). No effects of sex were observed. (d) Total
666 interaction time with the cylinders containing the mouse or rock. (n = 20 WT mice [8 male, 12 female], 24 KO

667 mice [10 male, 14 female]; two-way ANOVA [genotype x sex]). No effects of sex were observed. (e-f) Mean
668 interaction time per visit to (e) mouse or (f) rock cylinder (n = 20 WT mice [8 male, 12 female], 24 KO mice [10
669 male, 14 female]; two-way ANOVA [genotype x sex]; *$p<0.05$). No effects of sex were observed. (g-h) Total
670 interaction time with both objects during (g) training and (h) testing (n = 19 WT mice [9 male, 10 female], 19 KO
671 mice [11 male, 8 female]; two-way ANOVA [genotype x sex]). No effects of sex were observed.

672

673 **METHODS**

674 **Mice**

675 An H2BE-KO mouse was generated as described previously[1]. In brief, the endogenous H2BE CDS was replaced
676 with a membrane-targeted mCherry reporter sequence in C57Bl/6 mice. All mice were housed in a 12-hour light-
677 dark cycle and fed a standard diet. All experiments were conducted in accordance with and approval of the
678 IACUC.

679 **Histone extraction**

680 Snap-frozen brain tissues were homogenized in nuclear isolation buffer (NIB; 15mM Tris-HCl pH 7.5, 60mM KCl,
681 1mM $CaCl_2$, 15mM NaCl, 5mM $MgCl_2$, 250mM sucrose supplemented by protease inhibitor [Roche
682 04693124001], phosphatase inhibitor [Roche 04906837001], 1mM DTT, 1mM PMSF) + 0.3% NP-40 using a pre-
683 chilled dounce and pestle. Sample were then incubated on ice for 5 minutes, and centrifuged for 5 minutes at
684 1000g at 4°C. The pellet was washed 1x in NIB without NP-40 and centrifuged for 5 minutes at 1000g at 4°C. The
685 pellet was then resuspended in 1mL cold 0.4N H_2SO_4 and rotated overnight at 4C. Following the overnight
686 incubation, samples were pelleted for 5 minutes at 10,000g at 4°C and the supernatant was transferred to a
687 new tube. Trichloroacetic acid was added to 25% by volume, and the cells were left on ice at 4°C overnight. Cells
688 were again pelleted for 5 minutes at 10,000g at 4°C, and the supernatant was discarded. Samples were
689 centrifuged for 5 minutes at 16,000g at 4°C and supernatant was discarded. The pellet was washed 2X with ice-
690 cold acetone. After the second wash, samples were air-dried. The pellet was resuspended in molecular biology-
691 grade H_2O, sonicated in a Biorupter for 10 min, and then incubated at 50°C in a thermomixer shaking at
692 1000rpm. Samples were centrifuged for 10 minutes at 16,000g at 4°C and the supernatant containing the
693 histone fraction was collected.

694 **Western blotting**

695 Protein lysates or histone samples were mixed with 5X Loading Buffer (5% SDS, 0.3M Tris pH 6.8, 1.1mM
696 Bromophenol blue, 37.5% glycerol), boiled for 10 minutes, and cooled on ice. Protein was resolved by 16% Tris-
697 glycine SDS-PAGE, followed by transfer to a 0.45-µm PVDF membrane (Sigma-Aldrich IPVH00010) for
698 immunoblotting. Membranes were blocked for 1 hour at RT in 5% milk in 0.1% TBST and probed with primary
699 antibody overnight at 4C. Membranes were incubated with secondary antibody for 1 hour at RT. Antibodies are
700 shown in Supplemental Table.

701 **Immunohistochemistry**

702 *Brain sectioning*

703 Mice were anesthetized with isoflurane and transcardially perfused with 4% paraformaldehyde. Brains were
704 collected, rinsed with ice-cold PBS, placed in 15% sucrose solution at 4°C and allow to settle to the bottom.
705 Brains were then transferred to a 30% sucrose and again allowed to settle to the bottom. Brains were then
706 cryopreserved in O.C.T. Brains were coronally sectioned at 10µm using a cryostat and mounted on Superfrost
707 Plus slides.

708 *Staining*

709 Sections were washed 3X at RT in ash buffer (0.3% Triton X-100 in 1X PBS), then blocked at RT for 1h in Blocking
710 buffer (5% normal goat serum, 0.3% Triton X-100, 1% BSA in 1X PBS). Sections were washed 3X, then incubated
711 with primary antibody (diluted in Antibody Dilution buffer [0.3% Triton X-100, 1% BSA inX PBS]) in a humid
712 chamber overnight at 4°C. Sections were washed 3X, then incubated with secondary antibody (diluted in
713 Antibody Dilution buffer) in a humid chamber for 2h at RT. After three additional washes, sections were
714 incubated with 1ug/uL DAPI (Thermo Scientific 62247) for 10 min at RT. Coverslips were mounted onto slides
715 using Prolong Gold mounting medium. Slides were imaged on a Leica DM IL microscope with a 40X objective.

716 **Quantitative mass spectrometry**

717 *In-Solution Digestion*

718 Samples were solubilized and digested per the S-Trap Micro (Protifi) manufacturer's protocol[2]. Briefly, samples
719 were solubilized in 50 µL of extraction buffer containing 5% sodium dodecyl sulfate (SDS, Affymetrix), 50mM
720 TEAB (pH 8.5, Sigma), and protease inhibitor cocktail (Roche cOmplete, EDTA free), reduced in 5mM TCEP
721 (Thermo), alkylated in 20mM iodoacetamide (Sigma), then acidified with phosphoric acid (Aldrich) to a final
722 concentration of 1.2%. Samples were diluted with 90% methanol (Fisher) in 100 mM TEAB, then loaded onto an
723 S-trap column and washed three times with 50/50 chloroform/methanol (Fisher) followed by three washes of
724 90% methanol in 100 mM TEAB. A 1:10 ratio (enzyme: protein) of Trypsin (Promega) and LysC (Wako) suspended
725 in 20µL 50mM TEAB was added, and samples were digested for 1.5 hours at 47 °C in a humidity chamber. After
726 incubation, peptides were eluted with an additional 40 µL of 50 mM TEAB, followed by 40 µL of 0.1%
727 trifluoroacetic acid (TFA) (Pierce) in water, and finally 40 µL of 50/50 acetonitrile:water (Fisher) in 0.1% TFA.
728 Eluates were combined and desalted directly using Phoenix peptide cleanup kit (PreOmics) per manufactures
729 protocol, dried by vacuum centrifugation and reconstituted in 0.1% TFA containing iRT peptides (Biognosys,
730 Schlieren, Switzerland).

731 *Target Assay Development*

732 Parallel Reaction Monitoring (PRM) assay[3,4] was developed using target peptides identified from data
733 dependent acquisition (DDA) analysis of recombinant murine histone H2BE- and a tryptic digest of enriched
734 murine histones. A peptide unique to H2BE (EIQTSVR) and a peptide common to other H2B variants (EIQTAVR)
735 were selected. Heavy isotope-labelled peptides were synthesized, quantified by amino acid analysis, aliquoted,
736 and lyophilized by JPT Peptide Technologies, Berlin. To test and optimize the PRM method, 8ng of heavy isotope
737 peptides were initially spiked into 250ng of tryptic E.coli digest and injected on column. After PRM method
738 optimization, heavy labelled peptides were spiked into 2ug Histone tryptic so that 5ng was injected on column
739 for each peptide.

740 *Mass Spectrometry Data Acquisition*

741 Samples were analyzed on a Q-Exactive HF mass spectrometer (Thermofisher Scientific San Jose, CA) coupled
742 with an Ultimate 3000 nano UPLC system and an EasySpray source. Peptides were loaded onto an Acclaim
743 PepMap 100 75um x 2cm trap column (Thermo) at 5uL/min and separated by reverse phase (RP)-HPLC on a
744 nanocapillary column, 75 µm id × 50cm 2um PepMap RSLC C18 column (Thermo). Mobile phase A consisted of
745 0.1% formic acid and mobile phase B of 0.1% formic acid/acetonitrile. Peptides were eluted into the mass
746 spectrometer at 300 nL/min with each RP-LC run comprising a 90-minute gradient from 3% B to 45% B.

747 The mass spectrometer was set to repetitively scan m/z from 300 to 1400 (R = 240,000) followed by data-
748 dependent MS/MS scans on the twenty most abundant ions, minimum AGC 1e4, dynamic exclusion with a
749 repeat count of 1, repeat duration of 30s, and resolution of 15000. The AGC target value was 3e6 and 1e5, for
750 full and MSn scans, respectively. MSn injection time was 160 ms. Rejection of unassigned and 1+,6-8 charge
751 states was set.

752 The parallel reaction monitoring (PRM) method[3,4] combined two scan events. For the full scan we used 150–
753 2000 m/z mass selection, resolution 120,000 at m/z 200, automatic gain control (AGC) target value of 3e6, and
754 maximum injection time of 200ms. The targeted MS/MS was run at an Orbitrap resolution of 30,000 at m/z 200,
755 an AGC target value of 5e6, and maximum fill time of 200ms. and a target isolation window of 1.2 m/z.
756 Fragmentation was performed with normalized collision energy (NCE) of 27 eV. Table 1 shows targeted inclusion
757 list with scheduled retention times for heavy and light versions of EIQTAVR and EIQTSVR., along with
758 unscheduled acquisition of iRT peptides for internal quality control.

759 Table 1. The PRM scheduled list for heavy and light peptides

Mass [m/z]	Formula [M]	Species [z]	Polarity	Start[min]	End[min]	N(CE)	MSX	ID	Comment

408.73233		2	Positive	25	35	27			EIQTAVR(light)
413.73647		2	Positive	25	35	27			EIQTAVR(heavy)
416.72979		2	Positive	25	35	27			EIQTSVR(light)
421.73393		2	Positive	25	35	27			EIQTSVR(heavy)

760

761 *System Suitability and Quality Control*

762 The suitability of Q Exactive HF instrument was monitored using QuiC software (Biognosys, Schlieren,
763 Switzerland) and Skyline[5] for the analysis of the spiked-in iRT peptides in each sample. Meanwhile, as a measure
764 for quality control, we injected standard *E. coli* protein digest prior to and after injecting sample set and
765 collected the data in the Data Dependent Acquisition (DDA) mode. The collected data were analyzed in
766 MaxQuant[6] and the output was subsequently visualized using the PTXQC[7] package to track the quality of the
767 instrumentation.

768 *MS data processing and analysis*

769 The raw files for DDA analysis were processed with MaxQuant version 2.0.1.0 using its default workflow. The
770 reference *E. coli* proteome from UniProt was concatenated with murine histones and common protein
771 contaminants and used for the raw data search.

772 Skyline 21.2.0.568 with its default settings was used to process the PRM raw data. The heavy-isotope label for
773 the C-terminal Arg was set as static modification. All peak integrations were reviewed manually and the sum of
774 all transitions was calculated for light and heavy peptides. For each sample, light/heavy peak area ratio was
775 calculated and multiplied by the known heavy peptide amount per injection to estimate the light peptide
776 abundance value.

777 **Primary neuronal culture**

778 Cortices were dissected from E16.5 C57BL/6J embryos and cultured in supplemented neurobasal medium
779 (Neurobasal [Gibco 21103-049], B27 [Gibco 17504044], GlutaMAX [Gibco 35050- 061], Pen-Strep [Gibco 15140-
780 122]) in TC-treated 12- or 6well plates coated with 0.05 mg/mL Poly-D-lysine (Sigma-Aldrich A-003-E). At 3-4
781 DIV, neurons were treated with 0.5 µM AraC. For all experiments using cultured cortical neurons, neurons were
782 collected at 12 DIV.

783 **CUT&Tag-sequencing**

784 *Library preparation & sequencing*

785 Input samples were 400K primary cortical neurons per biological replicate. CUT&Tag was performed according
786 to published protocols[8]. Prior to sequencing, library size distribution was confirmed by capillary electrophoresis
787 using an Agilent 4200 TapeStation with high sensitivity D1000 reagents (5067-5585), and libraries were
788 quantified by qPCR using a KAPA Library Quantification Kit (Roche 07960140001). Libraries were sequenced on
789 an Illumina NextSeq550 instrument (42-bp read length, paired end).

790 *Data processing and analysis*

791 Reads were mapped to *Mus musculus* genome build mm10 with Bowtie 2 (v2.4.5)[9]. Six million reads from each
792 biological replicate were subset and each condition was then merged across biological replicates (SAMtools[10]
793 v1.15). Heatmaps were generated using deepTools[11] (v3.5.1). Metaplots were generated using ngs.plot[12] (v2.63)
794 against the mouse genome. Peaks were called using MACS3[13] (v3.0.0b1) and annotated using Homer[14] (v4.10) .
795 For downstream analysis, we used a Peak Score cutoff of 25 and removed peaks that were assigned to 'ChrUn'
796 (unknown chromosome) by Homer. The R package GenomicDistributions[15] (v1.6.0) was used to analyze the
797 genomic distribution of peaks. IGV tools[16] (2.12.3) was used to generate genome browser views.

798 To compare CUT&Tag signal to gene expression, normalized read counts from RNA-sequencing of WT primary
799 neuronal cultures (see RNA-sequencing methods section) were used to generate gene lists by expression level.

800 Genes with base mean < 3 were defined as 'not expressed'. The remaining genes comprise the 'all expressed'
801 categorization, and these genes were further divided into 3-quantiles (by base mean) to define 'low expression',
802 'mid expression' and 'high expression'.

803 *Gene ontology*

804 For gene ontology analysis, gene names were assigned to peak coordinates using Homer. Peaks that were
805 annotated as 'intergenic', 'non-coding', and 'NA' by Homer were not included in GO analysis. PANTHER[17,18]
806 (v18.0) was used to perform an overrepresentation test against the biological process complete ontology using
807 default parameters. The *Mus musculus* genome was used as a background gene list. For conciseness and
808 visualization, parent terms were excluded and only the most specific GO terms were plotted.

809 **Dot Blot**

810 0.2-µm PVDF paper was emersed in methanol and placed on TBS-soaked filter paper. Peptides were dotted onto
811 the PVDF paper at serial dilutions and allowed to dry for 4 hours. The membrane was then wet in methanol
812 again and equilibrated in TBS before blocking for 1 hour in 3% non-fat dry milk dissolved in TBS. The membrane
813 was then incubated in antibody solution for 1 hour at room temperature and washed 3 times for five minutes
814 in TBS-T (TBS with 0.1% Tween-20) before incubation with secondary antibody for 1 hour. Following secondary,
815 the membrane was again washed 3 times for five minutes before imaging.

816 **Protein extraction**

817 Tissues were homogenized in 500uL RIPA buffer (10% sucrose, 1% SDS, 5mM HEPES pH 7.9, 10mM sodium
818 butyrate in MilliQ water supplemented by protease inhibitor [Roche 04693124001], phosphatase inhibitor
819 [Roche 04906837001], 1mM DTT, 1mM PMSF) using a pre-chilled dounce and pestle. Samples were then titrated
820 5x with a 26.3 gauge needle and centrifuged for 15 min at max speed at 4°C. Supernatant containing protein
821 lysates were transferred to a new tube.

822 **Chromatin Biochemistry Methods**

823 *DNA preparation for chromatin assembly*

824 Mononucleosome-sized 601 DNA was prepared by PCR amplification of a DNA template containing one copy of
825 the Widom 601 DNA sequence[19]. PCR products were then pooled and purified with a QIAquick PCR Purification
826 Kit (Qiagen), using water to elute from the final columns. Eluents were pooled, frozen, and lyophilized before
827 being resuspended in buffer TE (10 mM Tris-HCl pH 7.6, 0.1 mM EDTA), quantified by NanoDrop OneC, and
828 adjusted to a final concentration of approximately 1-1.5 g/L.

829 DNA templates used for chromatin fibers were prepared essentially as described before[20]. *E. coli* DH5α cells
830 were transformed with a pWM530 vector bearing 12 repeats of the Widom 601 nucleosome positioning
831 sequence with a 30 bp linker and used to inoculate 6 L of luria broth under ampicillin selection and grown at 37
832 °C for 18-24 hrs. Cultures were harvested and DNA purified using a Plasmid Giga Kit (Qiagen). Purified DNA was
833 resuspended in buffer TE and adjusted to a concentration of ~1 g/L. Plasmid was then digested with EcoRI and
834 EcoRV (NEB) overnight to generate linear chromatin templates (i.e., dslDNA or 601^{18}-L. Complete digestion was
835 determined by agarose gel electrophoresis in 1X TAE buffer. Next, digestion reactions were fractionated by PEG
836 6000-induced precipitation as described previously to separate the ~3.2 kb desired chromatin substrates from
837 the 200-300 bp plasmid backbone fragments[21]. Precipitated DNA was next resuspended in buffer TE, purified
838 by phenol/chloroform extraction, and precipitated with absolute ethanol as described[22]. DNA was finally
839 resuspended in buffer TE, quantified by NanoDrop OneC, and adjusted to a concentration of 1-1.5 g/L. Buffer
840 DNA was likewise prepared by digestion of a similar construct containing 8 repeats of the 155 bp mouse
841 mammary tumor virus (MMTV) weak nucleosome positioning sequence with EcoRV, PEG precipitation, and
842 phenol/chloroform extraction.

843 *Histone expression and purification*

844 Recombinant human histones were expressed and purified as previously described[19]. Briefly, H2A, H2B, H2BE,
845 H3.1, H4, and histone mutants H2B V39I and H2BE I39V were expressed in *E. coli* BL21(DE3) or C41(DE3)) cells
846 at 37 °C until reaching an OD_{600} of 0.6-0.8, before induction with 500 µM IPTG for 4 hours at 37 °C. Bacteria
847 were then harvested by centrifugation at 6000 x g for 25 minutes.

848 Cell pellets were resuspended in lysis buffer (200 mM NaCl, 20 mM Tris-HCl pH 7.6, 1 mM EDTA, 1 mM β-
849 mercaptoethanol) and then lysed via sonication. Lysate was cleared by centrifugation at 30,000 x g for 20
850 minutes and the remaining insoluble pellet was resolubilized in extraction buffer (6 M guanidine HCl, 1 mM DTT,
851 1x PBS, pH 7) and nutated at 4 °C overnight. The extraction was cleared by centrifugation at 30,000 x g for 40
852 minutes and filtered using a 0.45-micron syringe filter (Fisher Scientific). Filtered extraction was diluted 1:1 with
853 HPLC buffer A (0.1% trifluoroacetic acid (TFA) in water) before purification with reverse-phase HPLC on a 30-
854 70% buffer B (0.1% TFA in 90% acetonitrile and 10% water). Absorbance at 280 nm was used to observe desired
855 peaks and fractions were collected using an automated fraction collector. Purity of fractions was determined
856 using a quadrupole LC-MS. Fractions deemed pure were combined, lyophilized and stored at -80 °C.

857 *Histone octamer assembly*

858 To assemble histone octamers, monomeric core histones were resuspended in unfolding buffer (20 mM Tris-
859 HCl pH 7.6, 6 M guanidine hydrochloride, 1 mM DTT) and quantified by measuring A280 using a NanoDrop. Core
860 histones were next combined at the following stoichiometries to generate a slight excess of H2A/H2B dimer to
861 assist with subsequent purification: 1.05:1.05:1:1 H2A:H2B:H3:H4. Total protein concentration of the mixture
862 was adjusted to 1 g/L, and samples were dialyzed against octamer refolding buffer (10 mM Tris-HCl pH 7.6, 2 M
863 NaCl, 1 mM EDTA, 1 mM DTT) at 4 °C using 3.5K MWCO Slide-A-Lyzer dialysis cassettes. A total of three rounds
864 of dialysis against refolding buffer were performed, with the first exchange going overnight and the subsequent
865 two lasting at least 6 hrs.

866 Following the final dialysis, samples were harvested from dialysis cassettes, cleared by centrifugation, and
867 concentrated using 30K MWCO Amicon centrifugal filter units. Finally, samples were centrifuged at 17,0000 xg
868 for a minimum of 10 minutes at 4 °C before being injected onto an AKTA 25L FPLC instrument and resolved over
869 a SuperDex 200 10/300 Increase column, using octamer refolding buffer for the liquid phase. Fractions were
870 analyzed by SDS-PAGE on 12 % acrylamide gels, and those containing octamers were pooled and concentrated
871 using Amicon 30K MWCO centrifugal filter unites. Octamers were quantified by A280, adjusted to 50 % (v/v)
872 glycerol, and stored at -20 °C for future use.

873 *Chromatin reconstitution*

874 Nucleosome core particles (NCPs), linear nucleosome arrays, and circular nucleosome arrays were all prepared
875 by the same method of salt gradient dialysis with all steps at 4 °C. Substrate DNA and recombinant histone
876 octamers were combined in approximately equimolar quantities (with respect to the expected nucleosome load
877 of the DNA, i.e., 1 for mononucleosomal DNA, or 12 for chromatin arrays) with final buffer conditions identical
878 to octamer refolding buffer – 10 mM Tris-HCl pH 7.6, 2 M NaCl, 0.1 mM EDTA, 1 mM DTT. For nucleosome array
879 assemblies MMTV DNA was also added, but at a lower stoichiometry to act as a buffer that facilitates array
880 assembly without competing for octamer occupancy (0.2:1 MMTV:NCP). Optimal assembly stoichiometries
881 were determined empirically for all templates, with Octamer:DNA stoichiometries being approximately 1.2:1
882 for mononucleosomes and 1.6:1 for 601 nucleosome arrays.

883 Assembly reactions were combined and mixed by gentle pipetting, centrifuged for 5 min at 17,000 xg at 4 °C,
884 and then added to Slide-A-Lyzer Mini dialysis buttons pre-moistened in array initial buffer (10 mM Tris-HCl
885 pH7.6, 1.4 M NaCl, 0.1 mM EDTA, 1 mM DTT) and dialyzed against 200 mL of the same buffer for 1 hr. Next, a
886 peristaltic pump was used to transfer 350 mL of dilution buffer (10 mM Tris-HCl pH 7.6, 10 mM NaCl, 0.1 mM
887 EDTA, 1 mM DTT) to the samples in initial buffer with a flow rate of 0.5-1.0 mL/min. After all dilution buffer was
888 transferred, arrays were left to dialyze for at least 1 hr or up to overnight. Samples were next moved to a fresh

889 350 mL of dilution buffer and dialyzed for 6 hrs. Lastly, samples were moved 300 mL of fresh dilution buffer and
890 dialyzed for 1-2 hrs before harvesting.

891 Mononucleosome samples were simply pipetted out of dialysis buttons, centrifuged for 5 min at 17,000 xg, and
892 supernatant (in case any precipitation was present) was quantified, subject to EMSA to validate assembly
893 efficiency, and stored at 4 °C for up to 2 months. Chromatin array samples were similarly harvested to yield a
894 mixture of assembled chromatin fibers, MMTV mononucleosomes, and free MMTV DNA. To separate the
895 chromatin fibers, an equal volume of precipitation buffer (10 mM Tris-HCl pH 7.6, 10 mM NaCl, 10 mM $MgCl_2$)
896 was added to samples followed by a 20-minute incubation on ice. Next, samples were centrifuged for 10 minutes
897 at 17,000 xg. Supernatant was gently pipetted off samples to avoid disturbing the barely visible pellets, to which
898 a desired volume of array dilution buffer was next added. Pellets were left on ice for 10 minutes undisturbed to
899 allow for the gradual resuspension of chromatin pellets before being quantified. Finally, EMSA was used to
900 validate assemblies and harvests. Chromatin arrays were stored at 4 °C for up to one week before use.

901 *Electrophoretic mobility shift assays (EMSAs)*

902 Mononucleosome EMSAs were performed using polyacrylamide gel electrophoresis in 5 % acrylamide, 0.5 X TBE
903 gels. A solution of 1 M sucrose was used as a loading buffer (1:3 dilution) for nucleosome samples. Gels were
904 run for 30-40 minutes at a constant voltage of 130 V, stained with SYBR Gold dye diluted 1:10,000 in 0.5 X TBE
905 buffer for 5-10 minutes, and DNA migration was visualized on an Amersham AI600 imager (GE/Cytiva) using the
906 UV 312 nm channel. If needed, protein migration was visualized after DNA imaging by staining gels with Imperial
907 Protein Stain and visualized on the AI600 instrument in the colorimetric channel.

908 Chromatin array EMSAs were performed similarly, except with a different gel formulation. Agarose-
909 polyacrylamide gel electrophoresis (APAGE) gels were cast using the Mini-PROTEAN Tetra Handcast system (Bio-
910 Rad). Before combining gel-casting reagents, the gel-facing sides of the 1.5 mm spacer plates, short plates, and
911 10-well gel combs were lubricated with a thin layer of 50 % (v/v) glycerol. Next, ultrapure water, 50X TAE

912 (sufficient for a final concentration of 0.5 X), and powdered agarose (sufficient for a final concentration of 1 %
913 w/v) were heated until dissolved. This solution was rapidly combined with 40 % acrylamide (37.5:1 mono:bis)
914 solution (Bio-Rad) (sufficient for a final concentration of 2 %), APS (sufficient for 0.125 %), and TEMED (sufficient
915 for 0.04 %), and added into the assembled gel casting cassettes. Gels were allowed to cool and polymerize for
916 at least 1 hr. Once cool, gels were pre-run at 4 °C in 0.5 X TAE buffer for 3 hrs at 100 V. Next, chromatin samples
917 could be loaded onto gels using sucrose loading solution and the gels run for approximately 1 hr at 120 V at
918 room temperature before visualization as mononucleosome EMSAs.

919 *Atomic force microscopy*

920 DNA-protein complexes were imaged using an Asylum MFP 3D Bio AFM (Oxford Instruments, Goleta CA) with
921 an Olympus AC240TS probe in tapping mode at room temperature. The samples were prepared a suitable
922 concentration (0.5-1.0 ng/µL), then 40 uL of prepared samples were slowly deposited to a freshly cleaved AP-
923 mica for 5 minutes and rinsed with 1 mL ultrapure deionized water twice before being gently dried with UHP
924 argon gas.

925 AFM images were collected at a speed of 0.5-1 Hz at 512 × 512-pixel resolution, with an image size of 2 µm. For
926 analysis, raw images were exported into 8-bit grayscale Tiff images using the Asylum Research's Igor Pro
927 software and imported into FIJI/ImageJ (NIH) for detection of single particles and quantification of volume,
928 surface area, and volume/surface area ratio using as has been done previously for studies of chromatin
929 compaction via AFM[23]. In order to assess single chromatin particles, rather than potential clusters of multiple
930 fibers or residual MMTV mononucleosomes, only particles with volumes measuring between 2,000 and 15,000
931 nm^3 were included in analyses.

932 *Magnesium-dependent self-association assay*

933 Chromatin compaction was tested by magnesium-drive self-association as described previously[24]. Briefly, a
934 magnesium solution (100 mM $MgCl_2$, 10 mM Tris-HCl pH 7.6, 10 mM NaCl) was titrated into the sample solution

935 to raise the magnesium concentration in 0.5 mM increments. After each addition, samples were allowed to sit
936 on ice for 10 min and then centrifuged for an additional 10 min at 17,000 xg at 4 °C. The concentration of soluble
937 DNA from nucleosome arrays was measured by NanoDrop.

938 *Nucleosome differential scanning fluorimetry (DSF) assays*

939 Nucleosome stability was measured using a Protein Thermal Shift kit (Applied Biosystems) with the following
940 modifications. The assay was conducted at 10 μL volumes with 10X SYPRO Orange dye (Invitrogen) and
941 nucleosome dilution buffer (10 mM Tris-HCl pH 7.6, 100 mM NaCl, 0.1 mM EDTA, and 1 mM DTT) in 384-well
942 plates. Final nucleosome concentrations used were approximately 60 ng/μL of DNA. Fluorescence melt curve
943 data was acquired using a QuantStudio 5 Real-Time PCR System (Applied Biosystems) with the following
944 method: initial ramp rate of 1.6 °C/s to 25 °C with a 5-minute hold time at 25 °C, followed by a second ramp
945 rate of 0.05 °C/s to 99.9 °C with a 2-minute hold time at 99.9 °C. Melting temperatures were calculated using
946 the Protein Thermal Shift software (Applied Biosystems).

947 **ATAC-sequencing**

948 *Library preparation & sequencing*

949 Input samples were 400K primary cortical neurons per biological replicate. Neurons were collected by scraping
950 in cold lysis buffer (10 mM Tris-Cl (pH 7.5), 10 mM NaCl, 3 mM $MgCl_2$, 0.1% (vol/vol) NP-40, 0.1% (vol/vol)
951 Tween-20 and 0.01% (vol/vol) digitonin) and washed in wash buffer (10 mM Tris-Cl (pH 7.5), 10 mM NaCl, 3 mM
952 $MgCl_2$ and 0.1% (vol/vol) Tween-20). Transposition was performed with Tagment DNA TDE1 (Illumina,
953 15027865). Transposition reactions were cleaned with AMPure XP beads (Beckman, A63880), and libraries were
954 generated by PCR with NEBNext High-Fidelity 2× PCR Master Mix (NEB, M0541). Prior to sequencing, library size
955 distribution was confirmed by capillary electrophoresis using an Agilent 4200 TapeStation with high sensitivity
956 D1000 reagents (5067-5585), and libraries were quantified by qPCR using a KAPA Library Quantification Kit

957 (Roche 07960140001). Libraries were sequenced on an Illumina NextSeq550 instrument (42-bp read length,
958 paired end).

959 *Data processing and analysis*

960 Reads were mapped to *Mus musculus* genome build mm10 with Bowtie 2 (v2.4.5)[9]. Fifty million reads were
961 subsetted from each biological replicate and each condition was then merged across biological replicates
962 (SAMtools[10] v1.15). Heatmaps were generated using deepTools[11] (v3.5.1). Metaplots were generated using
963 ngs.plot[12] (v2.63) against the mouse genome. Peaks were called using MACS3[13] (v3.0.0b1) and annotated using
964 Homer[14] (v4.10) . For downstream analysis, we used a Peak Score cutoff of 25 and removed peaks that were
965 assigned to 'ChrUn' (unknown chromosome) by Homer. Differential ATAC peaks were called using DiffBind[25]
966 (v3.4.11). The following genomic regions were used as input data for DiffBind analysis: WT ATAC peak
967 coordinates from MACS3 (Fig 2d-g), H2BE binding site coordinates from MACS3 peak calling of CUT&Tag data
968 (Fig 2h-k), TSS coordinates +/- 500bp from mm10, enhancer regions from brain tissue[26]. IGV tools[16] (2.12.3) was
969 used to generate genome browser views.

970 To compare ATAC signal within different genomic regions, we subset H2BE binding sites based on their Homer
971 annotations into promoter ('promoter-TSS' in Homer), gene body ('exon' and 'intron' in Homer), and intergenic
972 ('intergenic' in Homer).

973 **Viral infection**

974 *Viral constructs*

975 The GFP control plasmid was obtained from Addgene, pLenti-CMV-MCS-GFP-SV-puro (Addgene plasmid 73582).

976 The H2BE and H2B constructs were generated as previously described[1] and were provided by the Dulac lab. The
977 H2B and H2BE coding sequences were then moved to the pLenti backbone through Gibson assembly. Primers
978 were designed through NEB Builder to separately amplify H2B or H2BE and the pLenti backbone. Each primer

979 contained a non-complementary region on its 5'-end that corresponded to approximately 10 bases on the other
980 template. PCR amplification was performed with Q5 High-Fidelity DNA Polymerase (NEB M0491S). Following
981 DPN1 digestion, fragments were ligated together using NEBuilder HiFi DNA Assembly Master Mix (NEB E2621S)
982 and transformed into NEB 5-alpha Competent *E. coli* cells (E2621S). Plasmid sequence was verified through
983 Plasmidsaurus long read sequencing.

984 The H2BE-I39V construct was generated by site-directed mutagenesis of the H2BE backbone using Pfu Turbo
985 HotStart DNA polymerase (Agilent, 600322-51), and primers were created using the DNA-based primer design
986 feature of the online PrimerX tool. Constructs were verified by Sanger sequencing.

987 *Lentiviral production*

988 HEK293T cells were cultured in high-glucose DMEM growth medium (Corning 10-013-CV), 10% FBS (Sigma-
989 Aldrich F2442-500ML), and 1% Pen-Strep (Gibco 15140-122). Calcium phosphate transfection was performed
990 with Pax2 and VSVG packaging plasmids. Viral media was removed 2 h after transfection and collected at 48 and
991 72 h later. Viral media was passed through a 0.45-µm filter and precipitated for 48 hours with PEG-it solution
992 (40% PEG-8000 [Sigma-Aldrich P2139-1KG], 1.2 M NaCl [Fisher Chemical S271-1]). Viral particles were pelleted
993 and resuspended in 200µL PBS.

994 *Neuronal infection*

995 At 10 DIV, neurons were transduced overnight with lentivirus containing the constructs described above. Virus
996 was removed the following day, and neurons were cultured for one additional day.

997 **RNA-sequencing**

998 *Library preparation & sequencing*

999 Input samples were 400 primary cortical neurons from 4 WT biological replicates and 4 KO biological replicates.
000 RNA was isolated using Zymo Quick-RNA Miniprep Plus Kit (R1057). Prior to library preparation, RNA integrity
001 was confirmed using an Agilent 4200 TapeStation with high sensitivity RNA reagents (5067-5579). Sequencing
002 libraries were prepared using the TruSeq Stranded mRNA kit (Illumina 20020595). Prior to sequencing, library
003 size distribution was confirmed by capillary electrophoresis using an Agilent 4200 TapeStation with high
004 sensitivity D1000 reagents (5067-5585), and libraries were quantified by qPCR using a KAPA Library
005 Quantification Kit (Roche 07960140001). Libraries were sequenced on an Illumina NextSeq1000 instrument (66-
006 bp read length, paired end).

007 *Data processing and analysis*

008 Reads were mapped to *Mus musculus* genome build mm10 with Star (v2.7.9a). The R packages DESeq2[27]
009 (v1.38.3) and limma (v3.54.2) via edgeR[28] (v3.40.2) were used to perform differential gene expression analysis.
010 We defined genes as differentially expressed where FDR < 0.05 and absolute fold change 1.25. Volcano plots
011 were generated using VolcaNoseR[29]. IGV tools[16] (2.12.3) was used to generate genome browser views.

012 *Gene ontology*

013 PANTHER[17,18] (v18.0) was used to perform an overrepresentation test against the biological process complete
014 ontology using default parameters. SynGO[30] was used for synaptic gene ontologies and overrepresentation
015 tests of differentially expressed genes. All expressed genes (defined as base mean 3) was used as a background
016 gene list. For conciseness and visualization, parent terms were excluded and only the most specific GO terms
017 were plotted.

018 **Single-nucleus Drop-sequencing (sNucDrop-seq)**

019 *Nuclei isolation*

020 Snap-frozen brain tissues were homogenized in 1mL Buffer A (0.25M sucrose, 50mM Tris-HCl pH7.4, 25mM KCl,
021 5mM $MgCl_2$ supplemented by EDTA-free protease inhibitor [Roche 4693159001]) using a pre-chilled dounce and
022 pestle. Homogenate was then transferred to a pre-chilled 15mL conical tube and mixed with 6mL Buffer B (2.3M
023 sucrose, 50mM Tris-HCl pH7.4, 25mM KCl, 5mM $MgCl_2$). An additional 2mL Buffer A was used to rinse leftover
024 homogenate from the dounce and combined with the sample. The homogenate was gently transferred to a pre-
025 chilled 15mL ultracentrifuge tube containing 2mL Buffer C (1.8M sucrose, 50mM Tris-HCl pH7.4, 25mM KCl,
026 5mM $MgCl_2$). Nuclei were pelleted at 100,000 x g for 1.5hr at 4C using a SWI41 rotor. The supernatant was
027 discarded and 1.5mL Buffer D (0.01% BSA in 1X PBS with 0.5U/uL RNase inhibitor [Lucigen 30281-2]) was gently
028 added to the nuclei pellet and incubated on ice 20min. The nuclei pellet were resuspended and the suspension
029 was transferred to a 1.5mL lo-bind tube.

030 *Library preparation and sequencing*

031 The single-nucleus suspensions were individually diluted to a concentration of 100 nuclei/mL in DPBS containing
032 0.01% BSA. Approximately 1.5 mL of this single-nucleus suspension was loaded for each sNucDrop-seq run. The
033 single-nucleus suspension was then co-encapsulated with barcoded beads (ChemGenes) using an Aquapel-
034 coated PDMS microfluidic device (mFluidix) connected to syringe pumps (KD Scientific) via polyethylene tubing
035 with an inner diameter of 0.38mm (Scientific Commodities) (Macosko et al., 2015). Barcoded beads were
036 resuspended in lysis buffer (200 mM Tris-HCl pH8.0, 20 mM EDTA, 6% Ficoll PM-400 (GE Healthcare/Fisher
037 Scientific), 0.2% Sarkosyl (Sigma-Aldrich), and 50 mM DTT (Fermentas; freshly made on the day of run) at a
038 concentration of 120 beads/mL. The flow rates for nuclei and beads were set to 4,000 mL/hr, while QX200
039 droplet generation oil (Bio-rad) was run at 15,000 mL/hr. A typical run lasts 20 min. Droplet breakage with
040 Perfluoro-1-octanol (Sigma-Aldrich), reverse transcription and exonuclease I treatment were performed, as
041 previously described[31], with minor modifications. For up to 120,000 beads, 200 µL of reverse transcription (RT)
042 mix (1x Maxima RT buffer (ThermoFisher), 4% Ficoll PM-400, 1 mM dNTPs (Clontech), 1 U/mL RNase inhibitor,
043 2.5 mM Template Switch Oligo (TSO: AAGCAGTGGTATCAACGCAGAGTGAATrGrGrG), and 10 U/ mL Maxima H

044 Minus Reverse Transcriptase (ThermoFisher)) were added. The RT reaction was incubated at room temperature
045 for 30min, followed by incubation at 42C for 120 min. To determine an optimal number of PCR cycles for
046 amplification of cDNA, an aliquot of 6,000 beads was amplified by PCR in a volume of 50 µL (25 µL of 2x KAPA
047 HiFi hotstart readymix (KAPA biosystems), 0.4 µL of 100 mM TSO-PCR primer (AAGCAGTGGTATCAACGCAGAGT,
048 24.6 µL of nuclease-free water) with the following thermal cycling parameter (95C for 3 min; 4 cycles of 98C for
049 20 sec, 65C for 45 sec, 72C for 3 min; 9 cycles of 98C for 20 sec, 67C for 45 sec, 72C for 3 min; 72C for 5 min,
050 hold at 4C). After two rounds of purification with 0.6x SPRISelect beads (Beckman Coulter), amplified cDNA was
051 eluted with 10 µL of water. 10% of amplified cDNA was used to perform real-time PCR analysis (1 µL of purified
052 cDNA, 0.2 µL of 25 mM TSO-PCR primer, 5 µL of 2x KAPA FAST qPCR readymix, and 3.8 µL of water) to determine
053 the additional number of PCR cycles needed for optimal cDNA amplification (Applied Biosystems QuantStudio 7
054 Flex). We then prepared PCR reactions per total number of barcoded beads collected for each sNucDrop-seq
055 run, using 6,000 beads per 50- µL PCR reaction, and ran the aforementioned program to amplify the cDNA for 4
056 + 10 to 12 cycles. We then tagmented cDNA using the Nextera XT DNA sample preparation kit (Illumina, FC-131-
057 1096), starting with 550 pg of cDNA pooled in equal amounts, from all PCR reactions for a given run. Following
058 cDNA tagmentation, we further amplified the tagmented cDNA libraries with 12 enrichment PCR cycles using
059 the Illumina Nextera XT i7 primers along with the P5-TSO hybrid primer
060 (AATGATACGGCGACCACCGAGATCTACACGCCTGTCCGCGGAAGCAGTGGTATCAACGCAGAGT*A*C)[32]. After
061 quality control analysis by Qubit 3.0 (Invitrogen) and a Bioanalyzer (Agilent), libraries were sequenced on an
062 Illumina NextSeq 500 instrument using the 75-cycle High Output v2 Kit (Illumina). We loaded the library at 2.0
063 pM and provided Custom Read1 Primer (GCCTGTCCGCGGAAGCAGTGGTATCAACGCAGAGTAC) at 0.3 mM in
064 position 7 of the reagent cartridge. The sequencing configuration was 20 bp (Read1), 8 bp (Index1), and 60 bp
065 (Read2).

066 *Preprocessing of sNucDrop-seq data*

067 Paired-end sequencing reads of sNucDrop-seq were processed using publicly available the Drop-seq Tools v1.12
068 software[32] with some modifications. Briefly, each mRNA read (read2) was tagged with the cell barcode (bases 1
069 to 12 of read 1) and unique molecular identifier (UMI, bases 13 to 20 of read 1), trimmed of sequencing adaptors
070 and poly-A sequences, and aligned using STAR v2.5.2a to the mouse reference genome assembly (mm10,
071 Gencode release vM13). Because a substantial proportion (~50%) of reads derived from nuclear transcriptomes
072 of mouse cortices were mapped to the intronic regions, the intronic reads were retained for downstream
073 analysis. A custom Perl script was used to retrieve both exonic and intronic reads mapped to predicted strands
074 of annotated genes[31]. Uniquely mapped reads were grouped by cell barcodes. Cell barcodes were corrected for
075 possible bead synthesis errors, using the DetectBeadSynthesisErrors program from the Drop-seq Tools v1.12
076 software. To generate digital expression matrix, a list of UMIs in each gene (as rows), within each cell (as
077 columns), was assembled, and UMIs within ED = 1 were merged together. The total number of unique UMI
078 sequences was counted, and this number was reported as the number of transcripts of that gene for a given
079 nucleus.

080 *Nuclei clustering and marker gene identification*

081 Raw digital expression matrices were combined and loaded into the R package Seurat. For normalization, UMI
082 counts for all nuclei were scaled by library size (total UMI counts), multiplied by 10,000 and transformed to log
083 scale. Nuclei with a relatively high percentage of UMIs mapped to mitochondrial genes (0.2) were discarded.
084 Moreover, nuclei with <=500 UMI or =5000 UMI, discarded, as were nuclei with <=250 genes. Only genes found
085 to be expressing in 10 cells were retained. The Seurat object was then normalized and transformed using the
086 Seurat functions NormalizeData and SCTransform for each genotype. The Seurat functions
087 SelectIntegrationFeatures (nfeatures = 3000), PrepSCTIntegration, FindIntegrationAnchors and IntegrateData
088 were used to integrate the datasets based on the top 3000 more variable features. Prior to clustering, we
089 performed principal component analysis using the RunPCA function and selected 30 principal components for
090 UMAP non-linear dimensional reduction. Based on UMAP, twenty clusters were identified using the Seurat

091 functions Find Neighbors (dim = 30) and FindClusters (resolution = 0.5). To identify marker genes for each
092 cluster, differential expression analysis was performed using the Seurat function FindAllMarkers. Differentially
093 expressed genes that were expressed at least in 25% cells within the cluster and with a fold change more than
094 0.25 (log scale) were considered to be marker genes. Marker gene analysis led to the identification of 15 cortical
095 neuron clusters (10 excitatory, 5 inhibitory), 1 subcortical neuron cluster, and 4 non-neuronal clusters.

096 *Differential gene expression analysis*

097 Differential gene expression analysis between WT an KO groups was performed using the Seurat function
098 FindMarkers (min.pct = .00001, logfc.threshold = 0) with a Wilcoxon Rank Sum test. Genes with an adjusted p-
099 value <.05 were considered differentially expressed between WT and KO.

100 *Gene ontology*

101 PANTHER[17,18] (v18.0) was used to perform an overrepresentation test against the biological process complete
102 ontology using default parameters. All genes detected by FindMarkers was used as a background gene list. For
103 conciseness and visualization, parent terms were excluded and only the most specific GO terms were plotted.

104 **Electrophysiology**

105 Mice were deeply anesthetized and trans-cardially perfused with ice-cold aCSF containing (in mM): 124 NaCl,
106 2.5 KCl, 1.2 HaH2PO4, 24 NaHCO3, 5 HEPES, 13 Glucose, 1.3 MgSO4, 2.5 CaCl2. After perfusion, the brain was
107 quickly removed, submerged and coronally sectioned on a vibratome (VT1200s, Leica) at 400 µm thickness in
108 ice-cold aCSF. Slices were transferred to NMDG based recovery solution at 32ºC of the following composition
109 (in mM): 92 NMDG, 2.5 KCl, 1.2 NaH2PO4, 30 NaHCO3, 20 HEPES, 25 Glucose, 5 Sodium ascorbate, 2 Thiourea,
110 3 Sodium pyruvate, 10 MgSO4, 0.5 CaCl2. After 12-15 minutes recovery, slices were transferred to room
111 temperature aCSF chamber (20-22ºC) and left for at least 1 hour before recording. Following recovery, slices

112 were placed in a recording chamber, fully submerged at a flow rate of 1.4~1.6 mL/min and maintained at 29-
113 30°C in oxygenated (95% O2, 5% CO2) aCSF, with 100µM Picrotoxin included.

114 In extracellular recordings, recording pipettes were fabricated by pulling borosilicate glass (World Precision
115 Instruments, TW150-3). These pipettes exhibited a tip resistance ranging from 4 to 5 MΩ when filled with an
116 aCSF. Stimulus pipettes were made by pulling theta glasses (TG150-4, Warner Instrument) and adjusting the tip
117 size to 30~50 um. For measurements of evoked post-synaptic response in Schaffer-collateral pathway,
118 Hippocampal layers were identified using IR-DIC optics (BX51, Olympus), with visual guidance. The stimulus
119 electrode was positioned on the surface of the striatum radiatum (s.r.) from the CA3 direction. A recording
120 electrode was placed on the postsynaptic site in CA1, opposite the stimulus electrode.

121 Brief electrical pulses (0.2ms) were delivered on each sweep to measure post-synaptic responses every 10
122 seconds. Once responses stabilized, the intensity of the stimulus was sequentially adjusted for input-output (I-
123 O) measurement. Voltage (V) ranges were from 3V to 30V in increments of 3V. We identified the field excitatory
124 post-synaptic potential (fEPSP) based on the temporal separation of the fiber volley, and then averaged
125 measured the fEPSP slope of the 10-90% range from baseline to peak. Ten responses at the same input were
126 averaged.

127 Recordings were performed using a MultiClamp 700B (Molecular Devices) and Igor7 (WaveMetrics; recording
128 artist addon, developed by Richard C Gerkin, github : https://github.com/rgerkin/recording-artist), filtered at
129 2.8 kHz and digitized at 10 kHz. Axon terminals were stimulated with brief (0.2 ms) pulses using isoflex isolator
130 (Voltage control). Data were analyzed using Igor7.

131 **Behavioral assays**

132 *Behavioral cohorts*

133 Male and female WT and KO mice were tested in the behavioral tests described below. Mice were 3-4 months
134 old at the onset of behavioral testing. One cohort of mice was used for olfaction, social choice, and fear
135 conditioning testing, in that order. A separate cohort of mice was used for NOR and T-maze testing. During
136 testing, the experimenter was blinded to genotype of the mice.

137 *Olfactory habituation/dishabituation test*

138 Mice were tested for olfactory habituation & dishabituation using a published protocol[33]. In brief, mice received
139 sequential presentations of cotton swabs scented with different odors in the following sequence: water,
140 almond, vanilla, same sex conspecific, opposite sex conspecific. Each odor was presented in three consecutive
141 trials for 2 min, with an intertrial interval of 1 min. Time spent interacting with each scented swab was manually
142 analyzed by three scorers who were blinded to sex and genotype.

143 *NOR/open field*

144 Novel object recognition and open field were performed as described in Korb 2015[34] and Korb 2017[35]. In brief,
145 mice were placed in an empty arena for 10 minutes for a habituation period that also served as an open field
146 assessment. One day later mice were habituated for an additional 2 min and briefly removed from the arena
147 while two identical objects (either a faucet, a plastic pyramid, a small fish figurine, or stacked Legos) were placed
148 in the box and mice were given 10 min to explore. On the following day, mice were returned to the box with
149 one object they had previously seen and one new object in place of the original object and were allowed to
150 explore for 10 min. All sessions were recorded using EthoVision software. Time spent interacting with each
151 object was manually analyzed. Discrimination index was calculated as (time with novel object − time with
152 familiar object)/(time with novel object + time with familiar object).

153 *3-chamber social choice assay*

154 The social choice test was carried out in a three-chambered apparatus, consisting of a center chamber and two
155 outer chambers. Before the start of the test and in a counter-balanced manner, one end chamber was

156 designated the social chamber, into which a stimulus mouse would be introduced, and the other end chamber
157 was designed the nonsocial chamber. Two identical, clear Plexiglas cylinders with multiple holes to allow for air
158 exchange were placed in each end chamber. In the habituation phase of the test, the experimental mouse freely
159 explores the three chambers with empty cue cylinders in place for 10 min. Immediately following habituation,
160 an age- and sex-matched stimulus mouse was placed in the cylinder in the social chamber while a rock was
161 simultaneously placed into the other cylinder in the nonsocial chamber. The experimental mouse was tracked
162 during the 10 min habituation and 10 min social choice phases. All testing was recorded, and videos were
163 analyzed using ANY-maze software.

164 *T-maze*

165 For T-maze testing mice were placed at the end of the center arm of a T shaped raised arena enclosed with
166 plexiglass. Mice were allowed to freely explore for 7 minutes. Entries into each arm were defined as the full
167 body of the mouse entering (not necessarily including the tail). A success was defined as a consecutive entry
168 into each of the 3 arms without returning to the arm that the mouse had been in immediately prior. Successful
169 triads over the total number of possible triads based on the total entries were calculated as correct triad/(total
170 entries - 2).

171 *Contextual and cued fear conditioning*

172 Mice were handled for 2 minutes each on 3 consecutive days immediately prior to the onset of testing. On
173 training day, mice were placed in individual chambers for 2 min followed by a loud tone lasting 30 s that co-
174 terminated with a 2-s, 1.25-mA foot shock. One minute later mice received another tone-shock pairing and were
175 then left undisturbed for an additional 1 min in the chamber before being returned to their home cage. Freezing
176 behavior, defined as no movement except for respiration, was determined before and after the tone-shock
177 pairings and scored by MedAssociates VideoFreeze software. To test for context-dependent learning, we placed
178 mice back into the same testing boxes 24 hr later for a total of 5 min without any tone or shock, and again

179 measured the total time spent freezing. Following an additional 24 hr, we tested for cue-dependent fear
180 memory by placing the mice into a novel chamber consisting of altered flooring, wall-panel inserts, and vanilla
181 scent. After 2 min in the chamber, the cue tone was played for a total of 3 min, and the total time spent freezing
182 during the presentation of this cue tone was recorded. Long-term contextual and cued fear memory were again
183 tested with the same protocol at 14 d (contextual) or 15d (cued) post-training.

184

185 **REFERENCES**

186 1. Santoro, S. W. & Dulac, C. The activity-dependent histone variant H2BE modulates the life span of
187 olfactory neurons. *eLife* **1**, e00070 (2012).

188 2. Zougman, A., Selby, P. J. & Banks, R. E. Suspension trapping (STrap) sample preparation method for
189 bottom-up proteomics analysis. *Proteomics* **14**, 1006–1000 (2014).

190 3. Peterson, A. C., Russell, J. D., Bailey, D. J., Westphall, M. S. & Coon, J. J. Parallel Reaction Monitoring for
191 High Resolution and High Mass Accuracy Quantitative, Targeted Proteomics. *Molecular & Cellular Proteomics*
192 **11**, 1475–1488 (2012).

193 4. Gallien, S. *et al.* Targeted proteomic quantification on quadrupole-orbitrap mass spectrometer. *Mol*
194 *Cell Proteomics* **11**, 1709–1723 (2012).

195 5. MacLean, B. *et al.* Skyline: an open source document editor for creating and analyzing targeted
196 proteomics experiments. *Bioinformatics* **26**, 966–968 (2010).

197 6. Tyanova, S., Temu, T. & Cox, J. The MaxQuant computational platform for mass spectrometry-based
198 shotgun proteomics. *Nat Protoc* **11**, 2301–2319 (2016).

199 7. Bielow, C., Mastrobuoni, G. & Kempa, S. Proteomics Quality Control: Quality Control Software for
200 MaxQuant Results. *J Proteome Res* **15**, 777–787 (2016).

201 8. S Kaya-Okur, H. *Bench top CUT&Tag v3*. https://www.protocols.io/view/bench-top-cut-amp-tag-
202 bcuhiwt6 (2020) doi:10.17504/protocols.io.bcuhiwt6.

203 9. Langmead, B. & Salzberg, S. L. Fast gapped-read alignment with Bowtie 2. *Nat Methods* **9**, 357–359
204 (2012).

205 10. Danecek, P. *et al.* Twelve years of SAMtools and BCFtools. *Gigascience* **10**, giab008 (2021).

206 11. Ramírez, F. *et al.* deepTools2: a next generation web server for deep-sequencing data analysis. *Nucleic*
207 *Acids Res* **44**, W160–W165 (2016).

208 12. Shen, L., Shao, N., Liu, X. & Nestler, E. ngs.plot: Quick mining and visualization of next-generation
209 sequencing data by integrating genomic databases. *BMC Genomics* **15**, 284 (2014).
210 13. Zhang, Y. *et al.* Model-based Analysis of ChIP-Seq (MACS). *Genome Biol* **9**, R137 (2008).
211 14. Heinz, S. *et al.* Simple combinations of lineage-determining transcription factors prime cis-regulatory
212 elements required for macrophage and B cell identities. *Mol Cell* **38**, 576–589 (2010).
213 15. Kupkova, K. *et al.* GenomicDistributions: fast analysis of genomic intervals with Bioconductor. *BMC*
214 *Genomics* **23**, 299 (2022).
215 16. Robinson, J. T. *et al.* Integrative genomics viewer. *Nat Biotechnol* **29**, 24–26 (2011).
216 17. Ashburner, M. *et al.* Gene Ontology: tool for the unification of biology. *Nat Genet* **25**, 25–29 (2000).
217 18. Gene Ontology Consortium *et al.* The Gene Ontology knowledgebase in 2023. *Genetics* **224**, iyad031
218 (2023).
219 19. Lowary, P. T. & Widom, J. New DNA sequence rules for high affinity binding to histone octamer and
220 sequence-directed nucleosome positioning. *Journal of Molecular Biology* **276**, 19–42 (1998).
221 20. Osunsade, A. *et al.* A Robust Method for the Purification and Characterization of Recombinant Human
222 Histone H1 Variants. *Biochemistry* **58**, 171–176 (2019).
223 21. Lis, J. T. Fractionation of DNA fragments by polyethylene glycol induced precipitation. *Methods*
224 *Enzymol* **65**, 347–353 (1980).
225 22. Dyer, P. N. *et al.* Reconstitution of Nucleosome Core Particles from Recombinant Histones and DNA. in
226 *Methods in Enzymology* vol. 375 23–44 (Elsevier, 2003).
227 23. Krzemien, K. M., Beckers, M., Quack, S. & Michaelis, J. Atomic force microscopy of chromatin arrays
228 reveal non-monotonic salt dependence of array compaction in solution. *PLoS ONE* **12**, e0173459 (2017).
229 24. Schwarz, P. M., Felthauser, A., Fletcher, T. M. & Hansen, J. C. Reversible Oligonucleosome Self-
230 Association: Dependence on Divalent Cations and Core Histone Tail Domains. *Biochemistry* **35**, 4009–4015
231 (1996).

232 25. Ross-Innes, C. S. *et al.* Differential oestrogen receptor binding is associated with clinical outcome in
233 breast cancer. *Nature* **481**, 389–393 (2012).
234 26. Wang, Y. *et al.* SEdb 2.0: a comprehensive super-enhancer database of human and mouse. *Nucleic*
235 *Acids Res* **51**, D280–D290 (2023).
236 27. Love, M. I., Huber, W. & Anders, S. Moderated estimation of fold change and dispersion for RNA-seq
237 data with DESeq2. *Genome Biol* **15**, 550 (2014).
238 28. Robinson, M. D., McCarthy, D. J. & Smyth, G. K. edgeR : a Bioconductor package for differential
239 expression analysis of digital gene expression data. *Bioinformatics* **26**, 139–140 (2010).
240 29. Goedhart, J. & Luijsterburg, M. S. VolcaNoseR is a web app for creating, exploring, labeling and sharing
241 volcano plots. *Sci Rep* **10**, 20560 (2020).
242 30. Koopmans, F. *et al.* SynGO: An Evidence-Based, Expert-Curated Knowledge Base for the Synapse.
243 *Neuron* **103**, 217-234.e4 (2019).
244 31. Hu, P. *et al.* Dissecting Cell-Type Composition and Activity-Dependent Transcriptional State in
245 Mammalian Brains by Massively Parallel Single-Nucleus RNA-Seq. *Molecular Cell* **68**, 1006-1015.e7 (2017).
246 32. Macosko, E. Z. *et al.* Highly Parallel Genome-wide Expression Profiling of Individual Cells Using
247 Nanoliter Droplets. *Cell* **161**, 1202–1214 (2015).
248 33. Yang, M. & Crawley, J. N. Simple Behavioral Assessment of Mouse Olfaction. *CP Neuroscience* **48**,
249 (2009).
250 34. Korb, E., Herre, M., Zucker-Scharff, I., Darnell, R. B. & Allis, C. D. BET protein Brd4 activates
251 transcription in neurons and BET inhibitor Jq1 blocks memory in mice. *Nat Neurosci* **18**, 1464–1473 (2015).
252 35. Korb, E. *et al.* Excess Translation of Epigenetic Regulators Contributes to Fragile X Syndrome and Is
253 Alleviated by Brd4 Inhibition. *Cell* **170**, 1209-1223.e20 (2017).
254

255

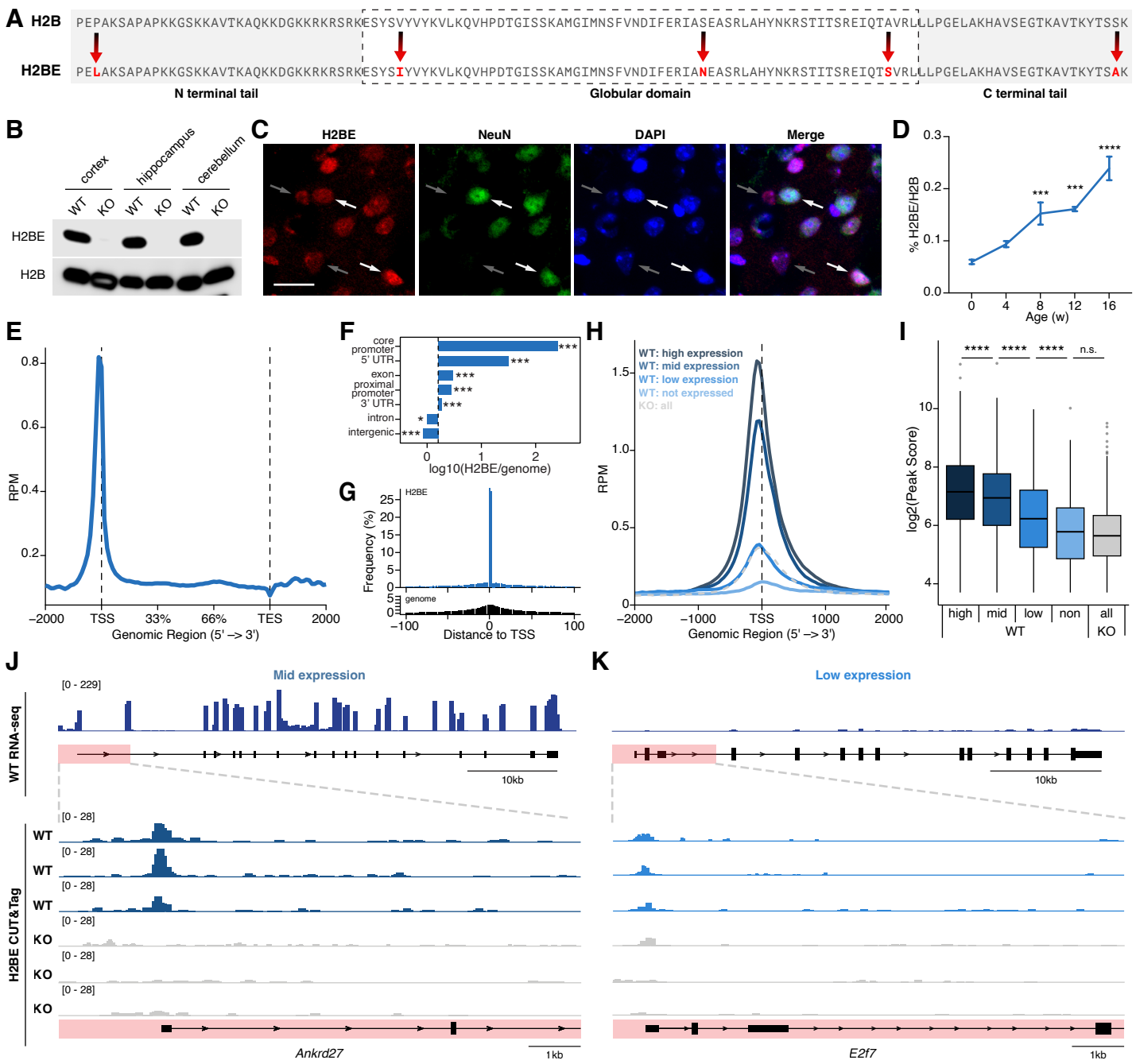
A
H2B
PEPAKSAPAPKKGSKKAVTKAQKKDGKKRKRSRKESYSVYVYKVLKQVHPDTGISSKAMGIMNSFVNDIFERIASEASRLAHYNKRSTITSREIQTAVRLLLPGELAKHAVSEGTKAVTKYTSSK
H2BE
PELAKSAPAPKKGSKKAVTKAQKKDGKKRKRSRKESYSIYVYKVLKQVHPDTGISSKAMGIMNSFVNDIFERIANEASRLAHYNKRSTITSREIQTSVRLLLPGELAKHAVSEGTKAVTKYTSAK
N terminal tail
Globular domain
C terminal tail
B
cortex
hippocampus
cerebellum
WT
KO
H2BE
H2B
C
H2BE
NeuN
DAPI
Merge
D
% H2BE/H2B
Age (w)
E
RPM
Genomic Region (5' –> 3')
TSS
33%
66%
TES
F
core promoter
5' UTR
exon
proximal promoter
3' UTR
intron
intergenic
log10(H2BE/genome)
G
H2BE
genome
Frequency (%)
Distance to TSS
H
WT: high expression
WT: mid expression
WT: low expression
WT: not expressed
KO: all
I
log2(Peak Score)
n.s.
high
mid
low
non
all
WT
KO
J
Mid expression
WT RNA-seq
[0 - 229]
10kb
H2BE CUT&Tag
[0 - 28]
Ankrd27
1kb
K
Low expression
E2f7

Figure 2

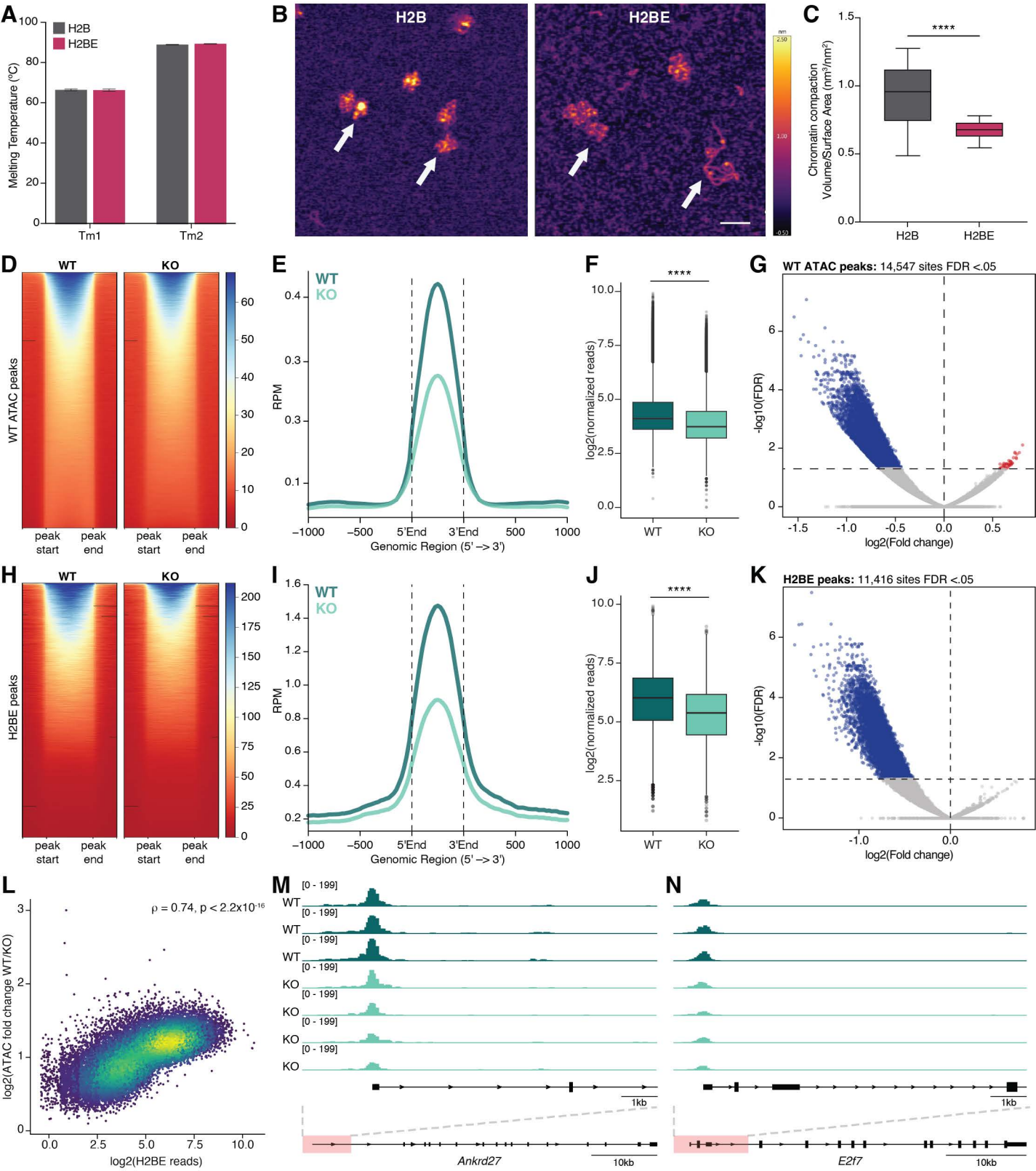
A
H2B
H2BE
Melting Temperature (°C)
Tm1
Tm2
B
H2B
H2BE
C
****
Chromatin compaction
Volume/Surface Area (nm³/nm²)
H2B
H2BE
D
WT
KO
WT ATAC peaks
peak start
peak end
E
WT
KO
RPM
Genomic Region (5' –> 3')
5'End
3'End
F
****
log2(normalized reads)
WT
KO
G
WT ATAC peaks: 14,547 sites FDR <.05
-log10(FDR)
log2(Fold change)
H
WT
KO
H2BE peaks
peak start
peak end
I
WT
KO
RPM
Genomic Region (5' –> 3')
J
****
log2(normalized reads)
WT
KO
K
H2BE peaks: 11,416 sites FDR <.05
-log10(FDR)
log2(Fold change)
L
ρ = 0.74, p < 2.2x10⁻¹⁶
log2(ATAC fold change WT/KO)
log2(H2BE reads)
M
[0 - 199]
WT
KO
1kb
Ankrd27
10kb
N
1kb
E2f7
10kb

Figure 3

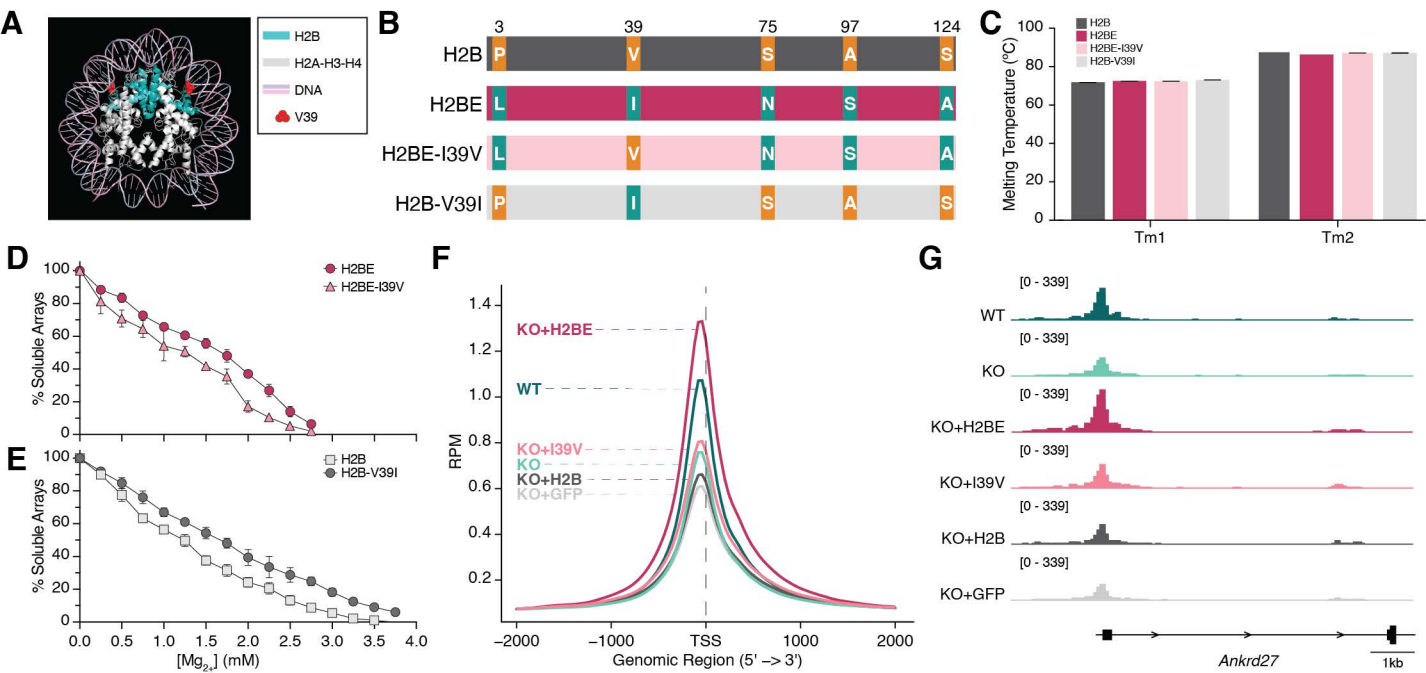
A
H2B
H2A-H3-H4
DNA
V39
B
3
39
75
97
124
H2B P V S A S
H2BE L I N S A
H2BE-I39V L V N S A
H2B-V39I P I S A S
C
H2B
H2BE
H2BE-I39V
H2B-V39I
Melting Temperature (°C)
Tm1
Tm2
D
H2BE
H2BE-I39V
% Soluble Arrays
E
H2B
H2B-V39I
% Soluble Arrays
[Mg2+] (mM)
F
KO+H2BE
WT
KO+I39V
KO
KO+H2B
KO+GFP
RPM
TSS
Genomic Region (5' –> 3')
G
[0 - 339]
WT
KO
KO+H2BE
KO+I39V
KO+H2B
KO+GFP
Ankrd27
1kb

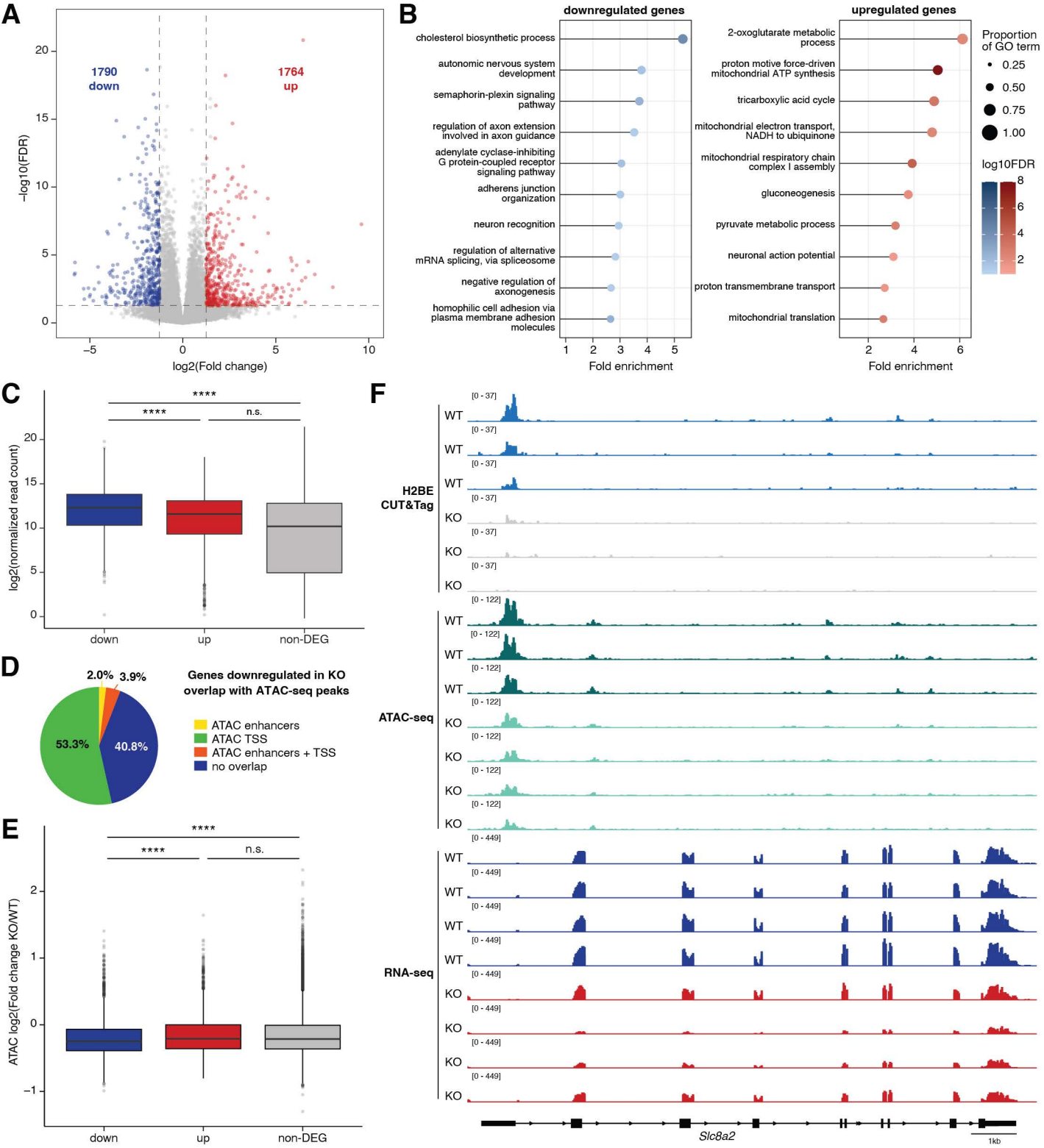
A
1790
down
1764
up
−log10(FDR)
log2(Fold change)
B
downregulated genes
cholesterol biosynthetic process
autonomic nervous system development
semaphorin-plexin signaling pathway
regulation of axon extension involved in axon guidance
adenylate cyclase-inhibiting G protein-coupled receptor signaling pathway
adherens junction organization
neuron recognition
regulation of alternative mRNA splicing, via spliceosome
negative regulation of axonogenesis
homophilic cell adhesion via plasma membrane adhesion molecules
Fold enrichment
upregulated genes
2-oxoglutarate metabolic process
proton motive force-driven mitochondrial ATP synthesis
tricarboxylic acid cycle
mitochondrial electron transport, NADH to ubiquinone
mitochondrial respiratory chain complex I assembly
gluconeogenesis
pyruvate metabolic process
neuronal action potential
proton transmembrane transport
mitochondrial translation
Fold enrichment
Proportion of GO term
0.25
0.50
0.75
1.00
log10FDR
C
****
****
n.s.
log2(normalized read count)
down
up
non-DEG
D
2.0%
3.9%
53.3%
40.8%
Genes downregulated in KO overlap with ATAC-seq peaks
ATAC enhancers
ATAC TSS
ATAC enhancers + TSS
no overlap
E
****
****
n.s.
ATAC log2(Fold change KO/WT)
down
up
non-DEG
F
H2BE CUT&Tag
ATAC-seq
RNA-seq
WT
KO
Slc8a2
1kb

Figure 5

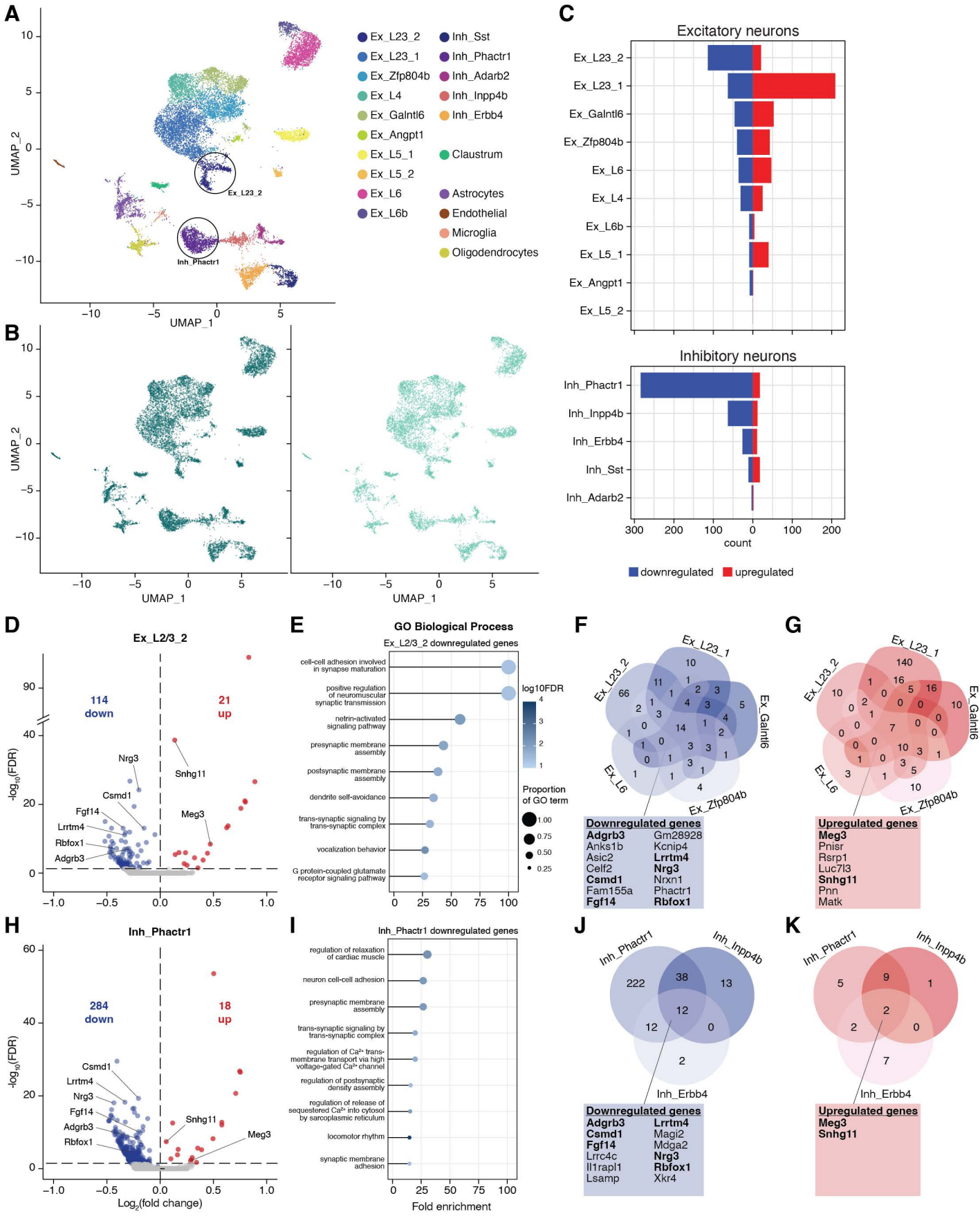
A
Ex_L23_2
Ex_L23_1
Ex_Zfp804b
Ex_L4
Ex_GalntI6
Ex_Angpt1
Ex_L5_1
Ex_L5_2
Ex_L6
Ex_L6b
Inh_Sst
Inh_Phactr1
Inh_Adarb2
Inh_Inpp4b
Inh_Erbb4
Claustrum
Astrocytes
Endothelial
Microglia
Oligodendrocytes
UMAP_1
UMAP_2
B
C
Excitatory neurons
Inhibitory neurons
count
downregulated
upregulated
D
Ex_L2/3_2
114 down
21 up
Nrg3
Csmd1
Fgf14
Lrrtm4
Rbfox1
Adgrb3
Snhg11
Meg3
-log10(FDR)
E
GO Biological Process
Ex_L2/3_2 downregulated genes
cell-cell adhesion involved in synapse maturation
positive regulation of neuromuscular synaptic transmission
netrin-activated signaling pathway
presynaptic membrane assembly
postsynaptic membrane assembly
dendrite self-avoidance
trans-synaptic signaling by trans-synaptic complex
vocalization behavior
G protein-coupled glutamate receptor signaling pathway
log10FDR
Proportion of GO term
F
Ex_L23_2
Ex_L23_1
Ex_GalntI6
Ex_L6
Ex_Zfp804b
Downregulated genes
Adgrb3 Gm28928
Anks1b Kcnip4
Asic2 Lrrtm4
Celf2 Nrg3
Csmd1 Nrxn1
Fam155a Phactr1
Fgf14 Rbfox1
G
Upregulated genes
Meg3
Pnisr
Rsrp1
Luc7l3
Snhg11
Pnn
Matk
H
Inh_Phactr1
284 down
18 up
Csmd1
Lrrtm4
Nrg3
Fgf14
Adgrb3
Rbfox1
Snhg11
Meg3
Log2(fold change)
I
Inh_Phactr1 downregulated genes
regulation of relaxation of cardiac muscle
neuron cell-cell adhesion
presynaptic membrane assembly
trans-synaptic signaling by trans-synaptic complex
regulation of Ca2+ trans-membrane transport via high voltage-gated Ca2+ channel
regulation of postsynaptic density assembly
regulation of release of sequestered Ca2+ into cytosol by sarcoplasmic reticulum
locomotor rhythm
synaptic membrane adhesion
Fold enrichment
J
Inh_Phactr1
Inh_Inpp4b
Inh_Erbb4
Downregulated genes
Adgrb3 Lrrtm4
Csmd1 Magi2
Fgf14 Mdga2
Lrrc4c Nrg3
Il1rapl1 Rbfox1
Lsamp Xkr4
K
Inh_Phactr1
Inh_Inpp4b
Inh_Erbb4
Upregulated genes
Meg3
Snhg11

Figure 6

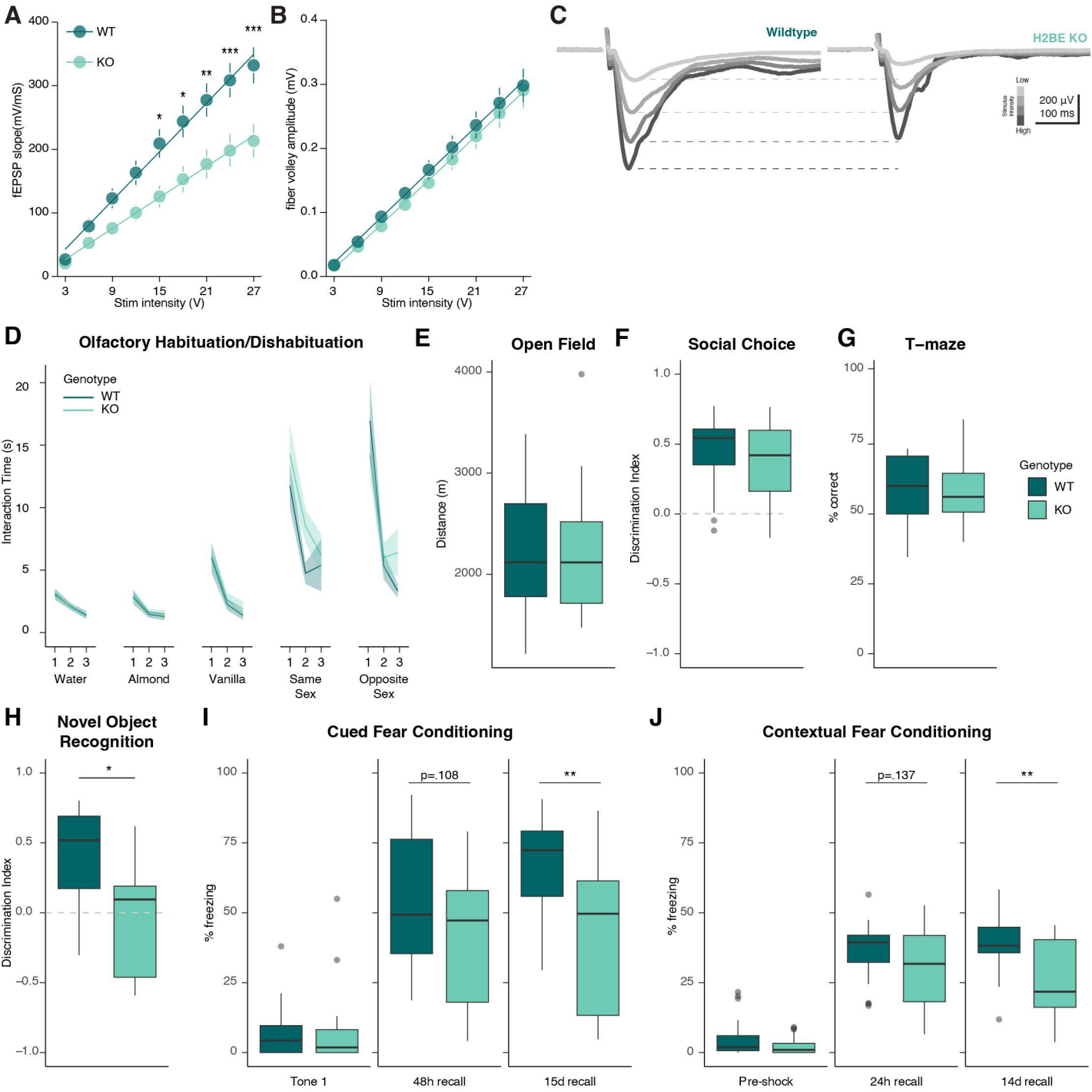
A
WT
KO
fEPSP slope(mV/mS)
Stim intensity (V)
B
fiber volley amplitude (mV)
Stim intensity (V)
C
Wildtype
H2BE KO
Low
High
200 µV
100 ms
D
Olfactory Habituation/Dishabituation
Genotype
WT
KO
Interaction Time (s)
Water
Almond
Vanilla
Same Sex
Opposite Sex
E
Open Field
Distance (m)
F
Social Choice
Discrimination Index
G
T–maze
% correct
Genotype
WT
KO
H
Novel Object Recognition
Discrimination Index
I
Cued Fear Conditioning
% freezing
p=.108
Tone 1
48h recall
15d recall
J
Contextual Fear Conditioning
% freezing
p=.137
Pre-shock
24h recall
14d recall

Figure 7

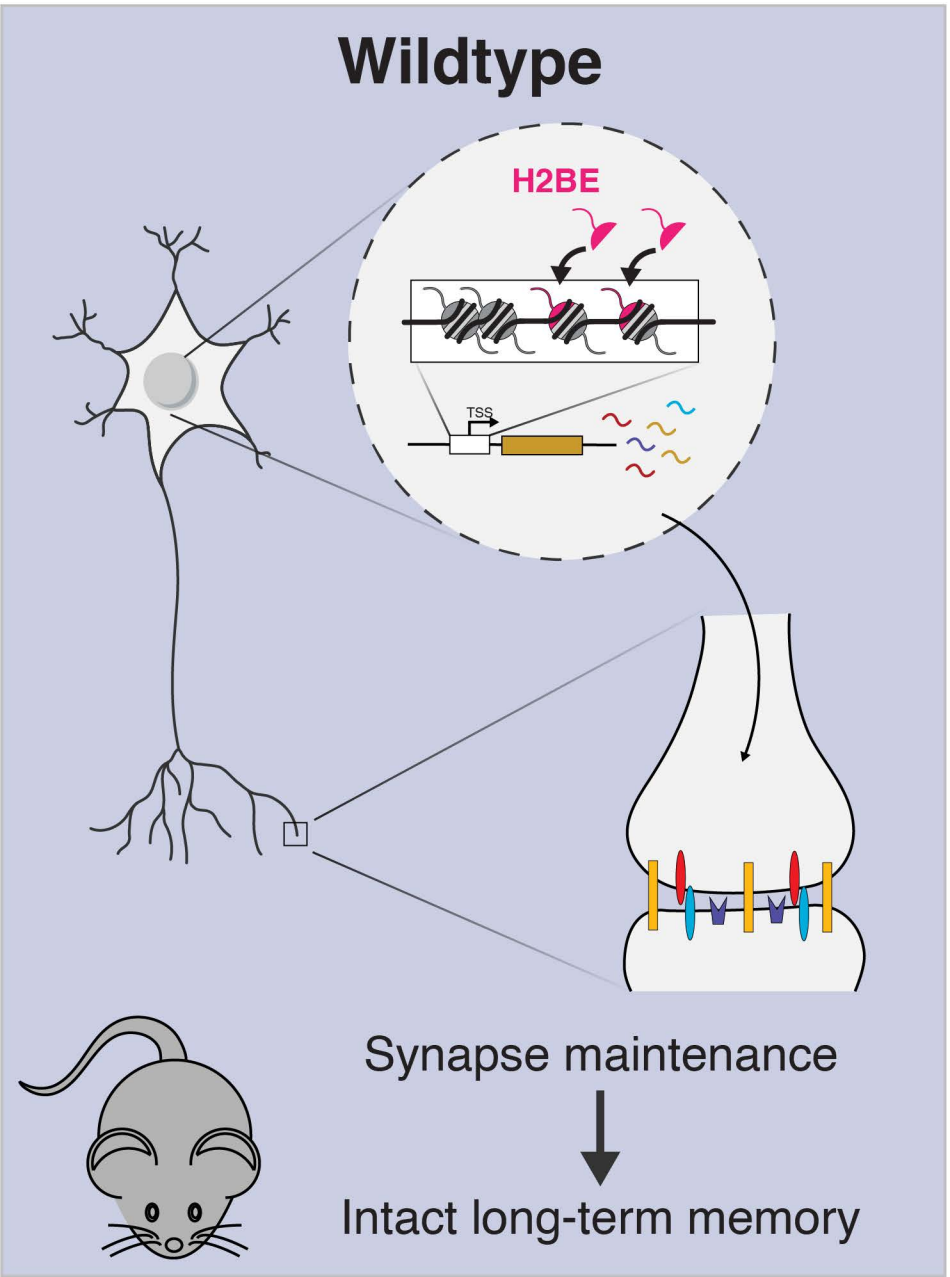
Wildtype
H2BE
TSS
Synapse maintenance
Intact long-term memory

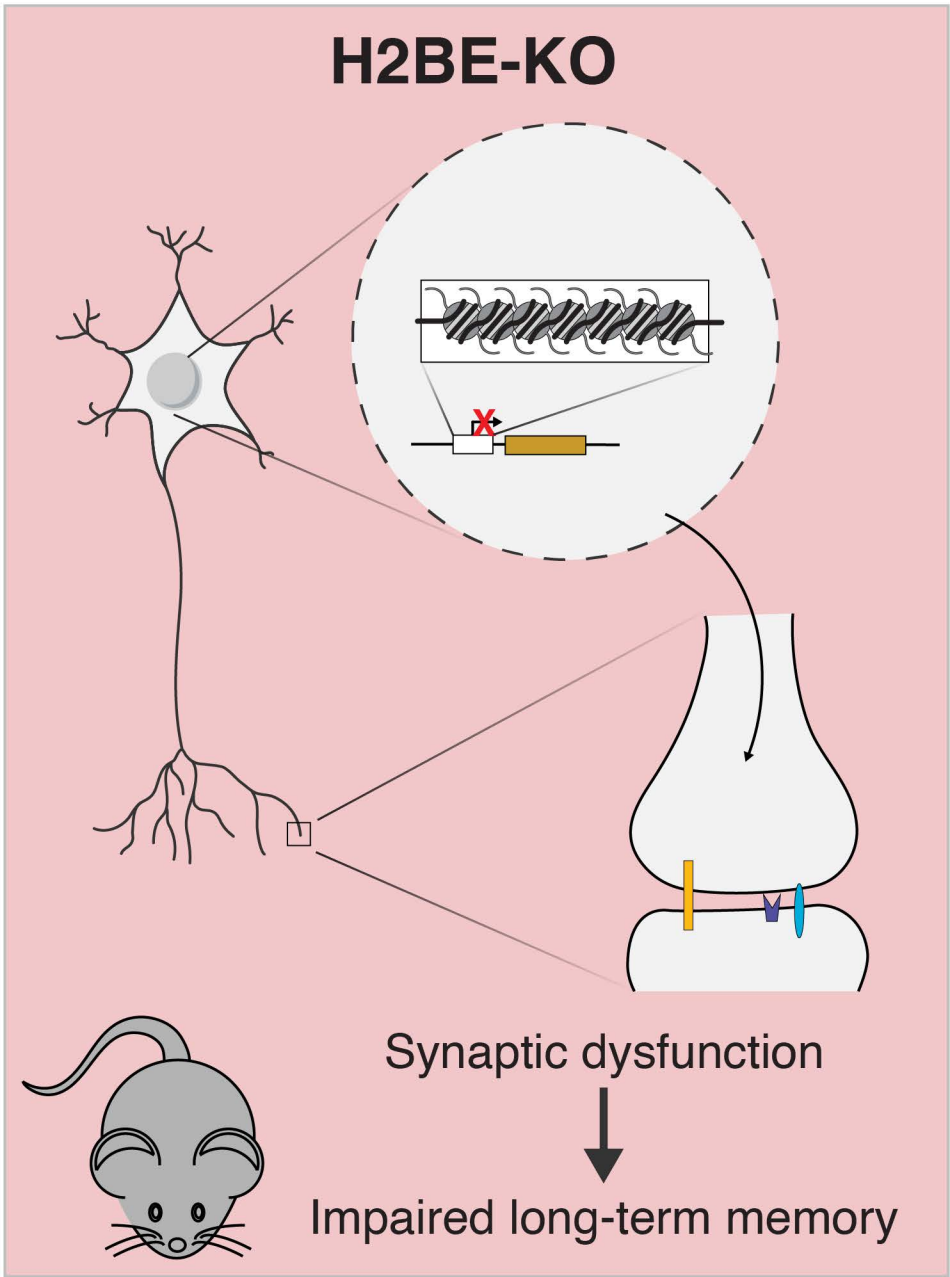
H2BE-KO
Synaptic dysfunction
Impaired long-term memory

Supplemental Figure 1

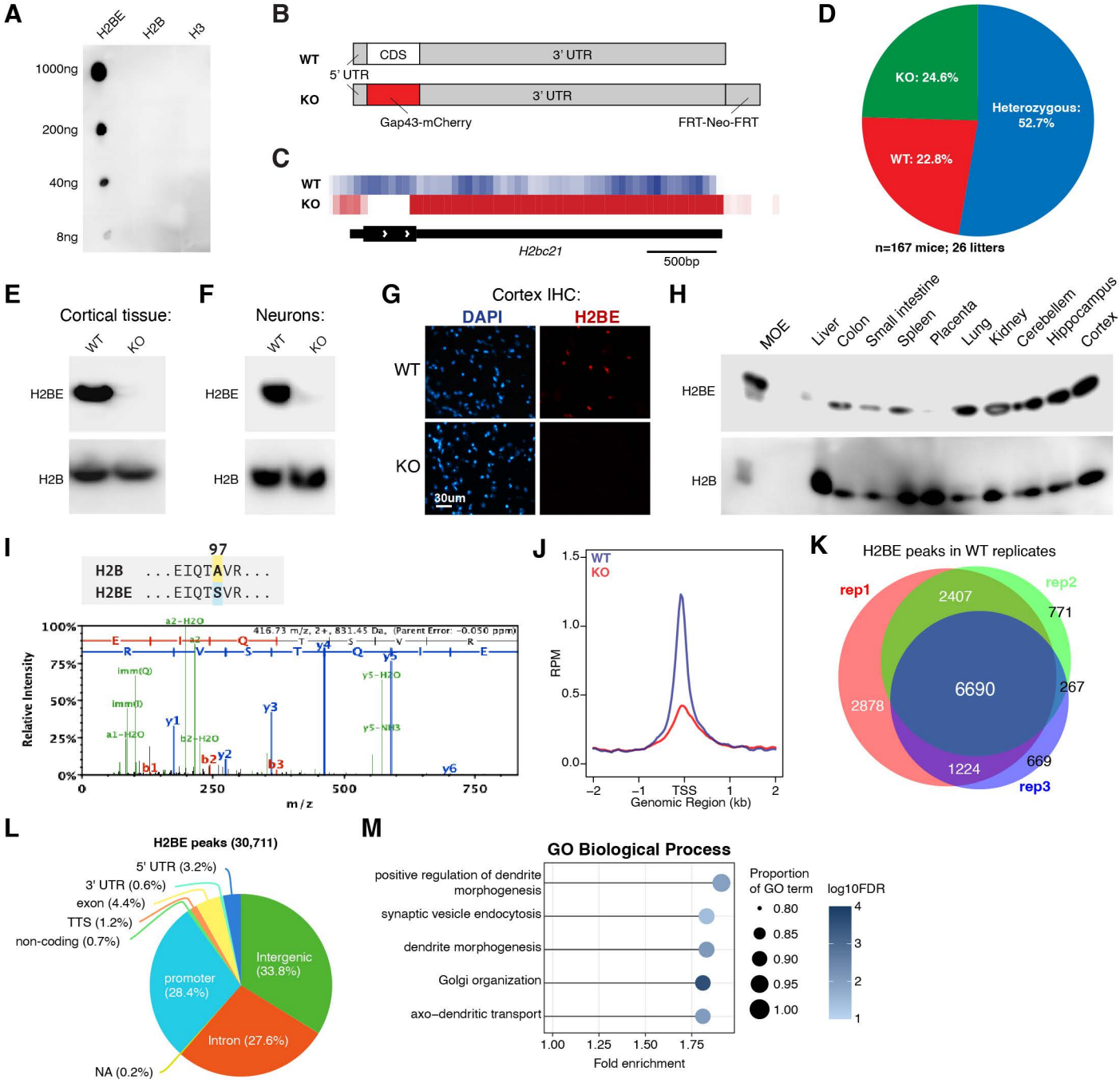

Supplemental Figure 2

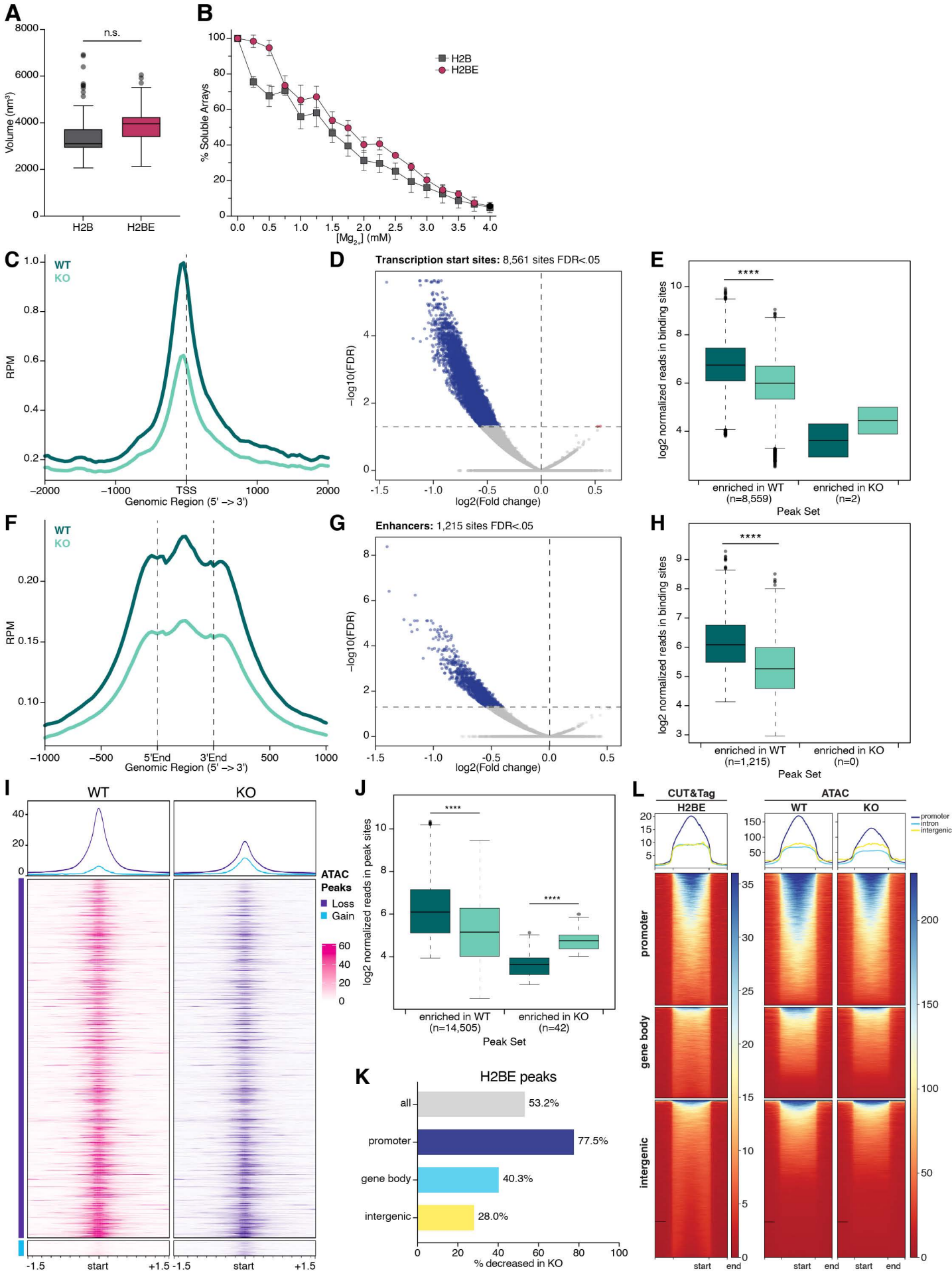

Supplemental Figure 3

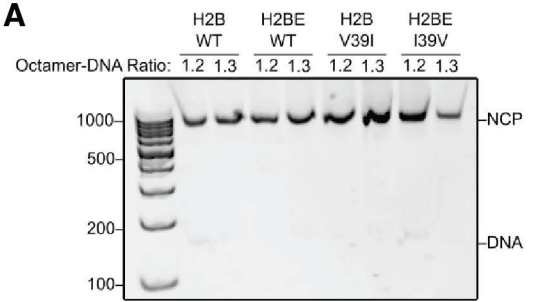

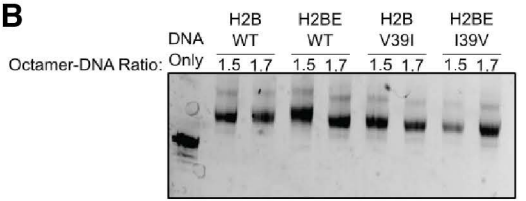

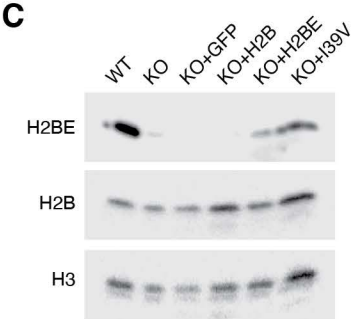

Supplemental Figure 4

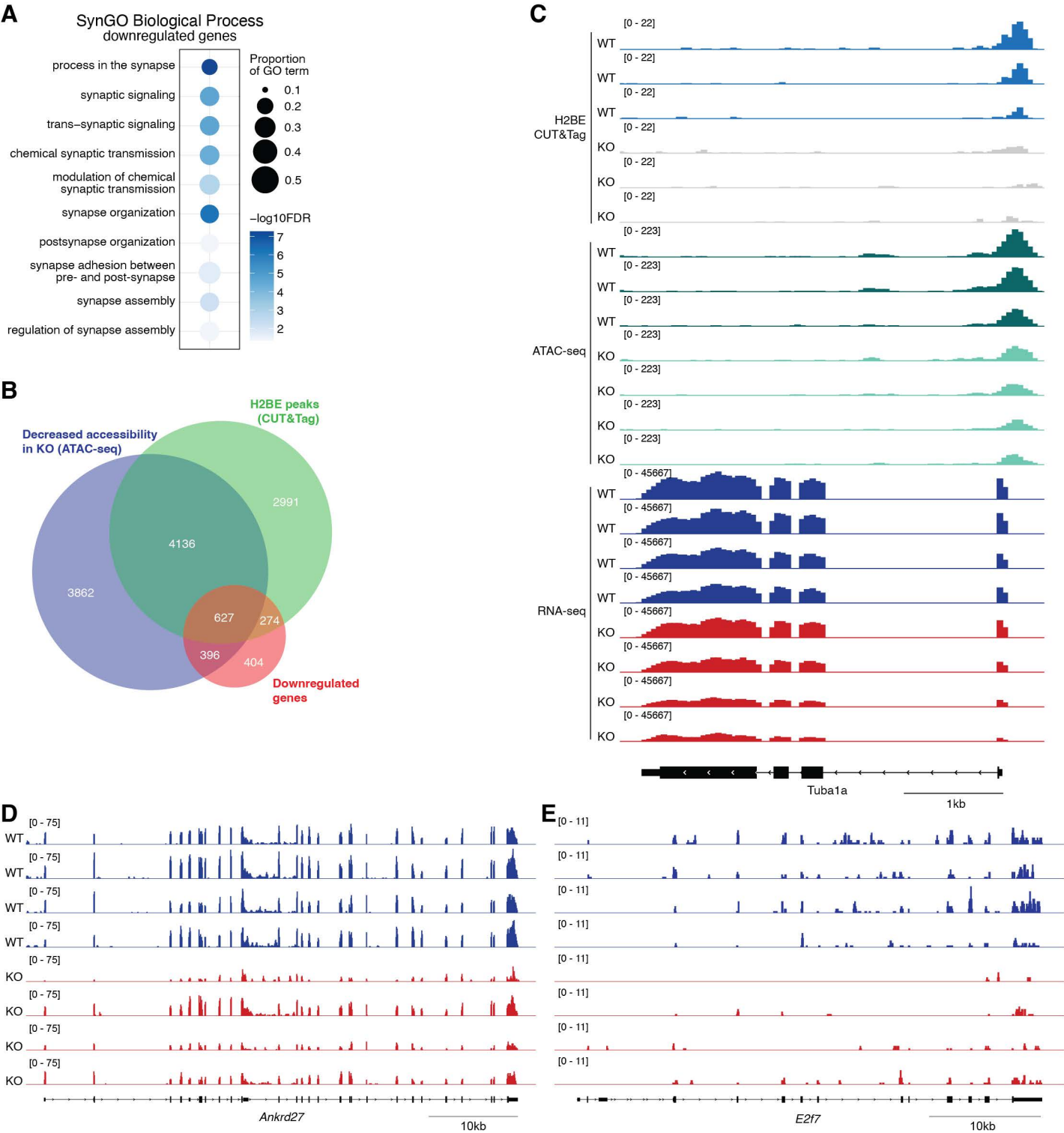

Supplemental Figure 5

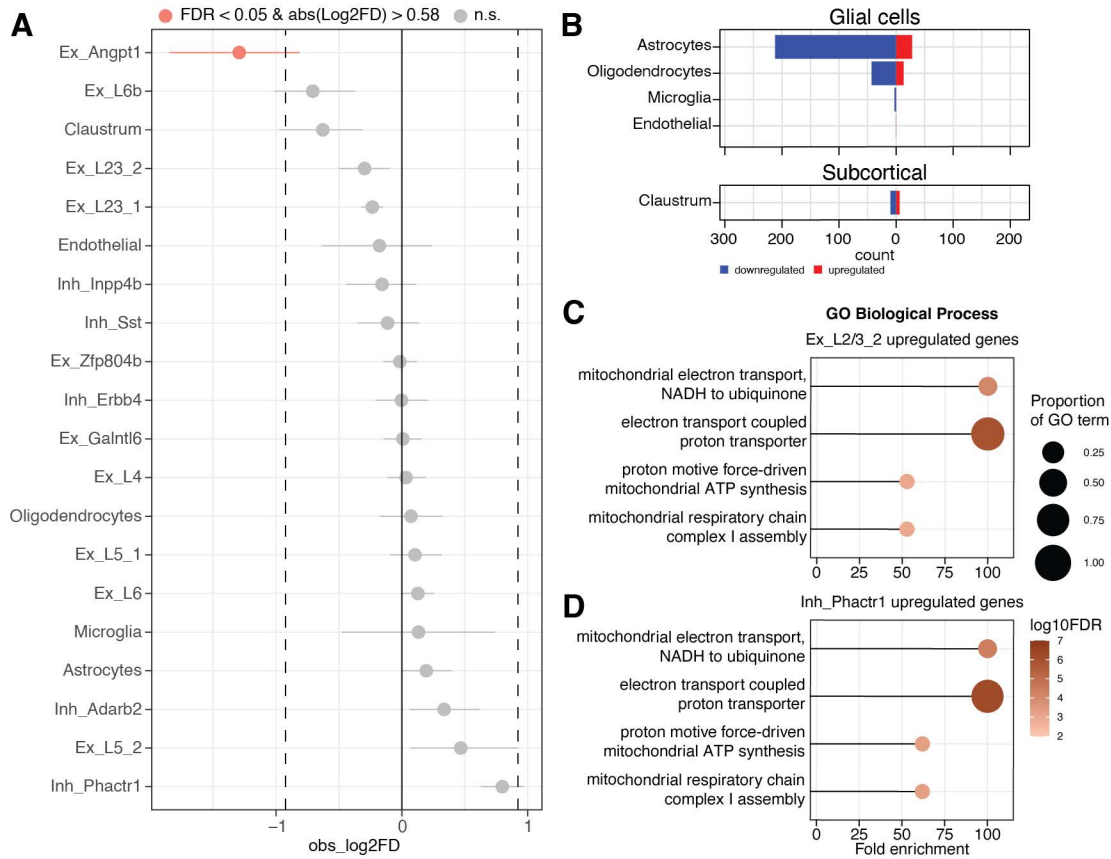
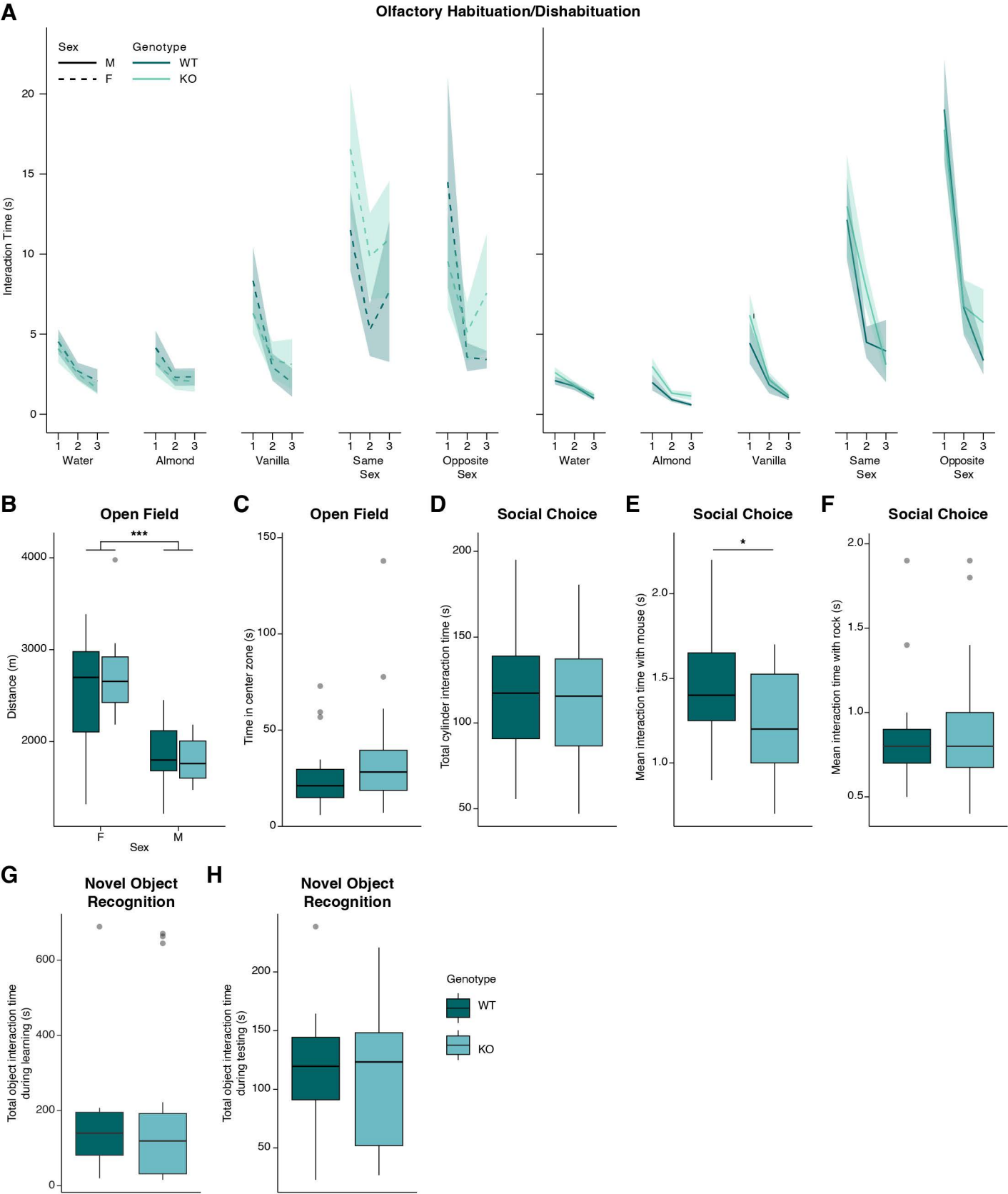
Supplemental Figure 6